Nanoscale

ROYAL SOCIETY OF CHEMISTRY

REVIEW

View Article Online
View Journal | View Issue

Check for updates

Cite this: *Nanoscale*, 2025, **17**, 7574

Recent advances in the fundamentals and *in situ* characterizations for mechanics in 2D materials

Hangkuan Ji, Zichen Song, An Wu, Yi-Chao Zou * and Guowei Yang

The growing need for integrating two-dimensional materials in electronic and functional devices requires the flexibility of the material. This necessitates the *in situ* characterization of their mechanical properties to understand their structure under stress loading in working devices. However, it is still challenging to directly characterize the mechanical behaviours of two-dimensional materials due to difficulties in handling these naturally fragile materials. In this review, we summarize the recent studies of mechanical properties in two-dimensional materials and their characterization using various microscopy techniques. This involves advances in fundamentals including the measurements of elastic properties, and the basic understanding of how structural parameters like defects and interfaces influence the deformation and failure process of two-dimensional materials. We also discuss the developed handling techniques for transferring two-dimensional materials to the characterization platforms, with the recent advances in *in situ* characterization studies based on atomic force microscopy and scanning/transmission electron microscopy. The above developments allowed the direct observation of unconventional mechanisms behind the deformation behaviour of two-dimensional materials, including plastic deformation, interlayer slip, phase transition and nanosized cracking. We then discuss the applications related to the mechanics of two-dimensional materials, including structural materials, electronic and optoelectronic properties, and further conclude with the opportunities and challenges in this field.

Received 8th December 2024,
Accepted 17th February 2025

DOI: 10.1039/d4nr05171h

rsc.li/nanoscale

1 Introduction

The isolation and identification of graphene in 2004[1] led to an explosion of interest in high-performance electronic and functional devices based on two-dimensional (2D) materials. Graphene itself is a strong and flexible conductor, and we now

School of Materials Science and Engineering, State Key Laboratory of Optoelectronic Materials and Technologies, Nanotechnology Research Center, Sun Yat-sen University, Guangzhou, 510275, P. R. China. E-mail: zouych5@mail.sysu.edu.cn

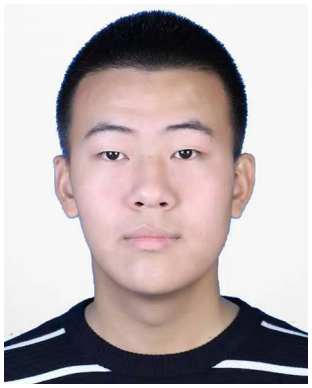

Hangkuan Ji

Hangkuan Ji is currently a graduate student at Sun-yat Sen University, pursuing his master's degree in the Department of Materials Science and Engineering at Sun-yat Sen University, China. His research interests include the functional applications of 2D minerals and their electron-microscopy characterization.

Yi-Chao Zou

Yi-Chao Zou is currently an associate professor at Sun-yat Sen University, China. She received her B.E. degree in Materials Science and Engineering from Central South University, and her Ph.D. degree from the University of Queensland, and subsequently worked as a postdoctoral researcher at the University of Manchester. She has published over 60 peer-reviewed papers in Nature Materials, ACS Nano, etc. Her research interests include the characterization and applications of 2D minerals and the design of 2D materials for in situ electron-microscopy characterization.

have 2D materials beyond graphene, with variable and tunable electronic and phonon structures.[2–5] For example, hexagonal boron nitride (*h*BN) is an insulator which can act as a dielectric,[6] and many materials in transition metal dichalcogenides (TMDs) are semiconductors that can be used as transistors,[4] optical absorbers,[7] and light emitters.[8] Because of the high mechanical flexibility,[9] chemical stability,[10] high mobility,[6] high transmittance,[11] strong light–material interactions,[7] electrochemical activity,[12,13] and large-scale processability,[14–17] 2D materials have nowadays been applied to flexible and wearable devices,[18–20] including electronic skin,[21] wearable heath monitors,[22,23] foldable screens[24] and phones,[25] and thermoelectric devices.[26]

During the applications, the intrinsic properties of 2D materials determine their device stability. Therefore, it is important to understand their intrinsic elastic properties, deformation and fracture mechanisms. To date, the number of reports on the mechanics of 2D materials has been increasing annually.[27–30] The corresponding characterization methods and instruments have made significant progress in determining mechanical properties that were not able to be measured experimentally before, such as the instability under stress loading,[31] the fatigue life[32] and the bending stiffness of heterostructures with complex 2D components.[33] Meanwhile, recent developments in the fundamentals of mechanics and the fabrication techniques of materials have allowed more controllability over the transfer, stacking and assembling of 2D materials.[34–38] This enables accessibility to a quantitative understanding of the mechanics of those thin samples that were too challenging to be handled before,[34] the construction of regularly aligned 2D composites with high flexibility and high stiffness,[38,39] as well as the unravelling of unusual deformation mechanisms[30] and new functionalities in 2D materials.[34,36] Therefore, a state-of-the-art review of the characterization and applications of 2D materials' mechanics will be greatly helpful for readers to understand the research status, outline the new challenges and establish potential research directions for future.

In this review, we summarize the mechanical properties and related characterization approaches for 2D materials, and discuss how these properties influence their real device applications. In section 2, we discuss the intrinsic mechanical properties of 2D materials, including elastic moduli, fracture strength and bending stiffness. In section 3, we emphasize the recent development in instruments for characterization studies of deformation behaviours, where the understanding of the material's response to dynamic stress is new for 2D materials. The inaccuracies that may occur during measurements shall also be proposed, which may lie in the sample preparations themselves (defects and contamination from sample transfers *etc.*) or in the mechanical loading and measuring approaches (model simplification, local stress or global stress, imaging resolution *etc.*), In section 4, we discuss materials parameters that influence the fracture mechanisms of 2D materials, including layer thickness, grain boundaries, defects and interfaces. Section 5 reviews the applications based on the mechanics of 2D materials. Starting with the rational design of structural materials consisting of 2D materials, we introduce the electronic properties that are related to the strain engineering of 2D materials, including the electronic, optoelectronics, and ferroelectric properties.[40,41] We then conclude with our prospects on the remaining challenges and opportunities that are potentially exciting for researchers.

2 Intrinsic mechanics of 2D materials

Elastic properties such as in-plane and out-of-plane elastic moduli describe the stretchability and reversibility of deformation of 2D materials, critical for their application in flexible devices. This section summarizes the mechanical properties of 2D materials that have been measured experimentally, including elastic modulus and fracture strength. The recent development in approaches for measuring bending stiffness is also reviewed.

2.1 Elastic modulus and fracture strength

The two-dimensional Young's modulus (E^{2D}) is one of the earliest reported mechanical properties of 2D materials measured by experiments. The mechanical properties of graphene were first measured by Lee *et al.* through nanoindentation using atomic force microscopy (AFM).[1,42] They revealed an E^{2D} of 340 N m^{-1} in graphene, which is then transformed to the standard (three-dimensional) 3D in-plane elastic modulus (effective Young's modulus) with the value of 1 TPa.[42] In fact, graphene is so tough that it shattered the standard silicon AFM tips, necessitating diamond tips.[42] Theoretically, the elastic deformation of graphene can reach ~20%,[42] giving a facture strength/Young's modulus ratio (σ_f/E) of ~10^{-1}, this being the largest among the current materials suitable for bendable devices (Fig. 1 and Table 1).[43]

Beginning with graphene, the fundamental elastic properties of many other 2D materials have been subsequently revealed. Specifically, the deformability of *h*BN and TMDs has been extensively studied.[44–47] This is because 2D electronic devices have aroused much research interest in recent decades, where *h*BN often acts as a dielectric layer and TMDs work as an active layer. It was found that, among the TMDs, MoS_2 exhibits a comparatively high value of the elastic modulus, which remains one of the most important components for flexible electronics.[33] For other types of metal chalcogenide, it was interesting to see that there are a few reported as highly deformable, where unexpected plasticity behaviour was observed,[48] including InSe, GaTe and $MoTe_2$.[30] Also, it should be noted that the phase structure of the crystals can lead to variable mechanical performance. For example, in $MoTe_2$, the breaking strengths of distorted 1T′ and T_d phases are only half the value of 2H-$MoTe_2$ phase due to the uneven distribution of bonding strengths.[49]

The high fracture strength measured from 2D materials requires high-quality samples, *e.g.* mechanical exfoliated

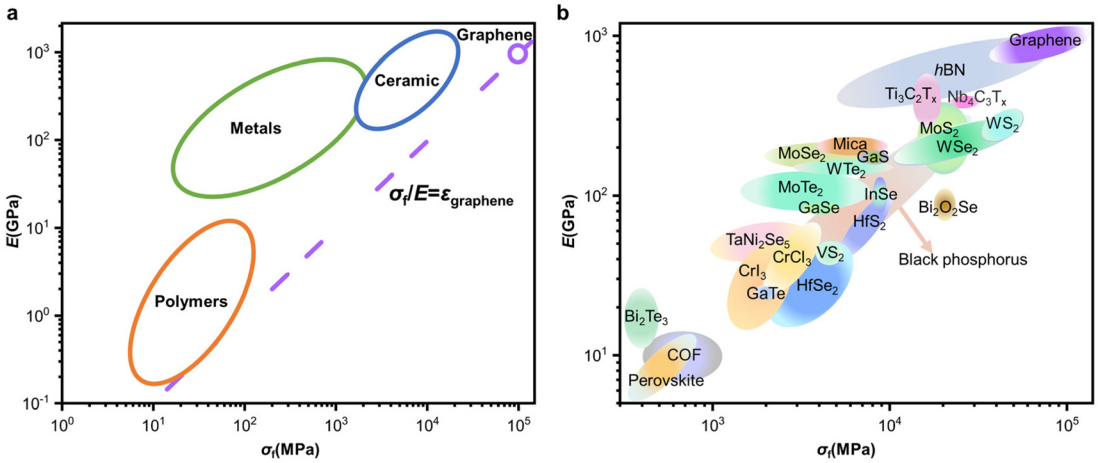

Fig. 1 (a) A material design plot comparing the failure strength with Young's moduli. Materials that maximize σ_f/E indicate that they can sustain a large elastic strain before fracture. Materials with σ_f/E smaller than graphene suggest that they are suitable for being integrated into graphene-based devices, as graphene cannot fracture during deformation.[43] (b) Comparison of the elastic modulus and failure strength of various 2D crystals.[28,29,34,42,44–47,49–83]

single crystals. Therefore, there is a discrepancy between the value from single crystals for fundamental studies and their nanobulk counterparts for scalable devices, where the large elasticity is no longer preserved. Demonstrated approaches to increase the deformability and strength of 2D materials shall be discussed further in the following sections.

2.2 Bending stiffness

The bending stiffness B governs the 3D deformation behaviours of 2D materials and directly describes their flexibility.[84,85] When the total bending stiffness reaches a theoretical minimum, the extreme deformability of 2D materials can be achieved. Recently, the bending stiffness of graphene and related heterostructures has been measured through characterizing the deformation geometry of pressurized bubbles[54] by atomic force microscopy (AFM), or curved 2D samples using cross-sectional scanning transmission electron microscopy (STEM) imaging.[86,87] Through using atomic-resolution STEM imaging, Zande *et al.* studied the bending stiffness of graphene flakes as a function of layer number N, using the deformed geometry of the graphene that was transferred onto the *h*BN step edge. This generates a local region subjected to bending stress (Fig. 2a–d), where the curvature of the bent graphene and the step height of the *h*BN edges can be measured from the cross-sectional STEM images. They further calculate the bending stiffness using:

$$B = R\Gamma\left(\frac{H - 2R(1-\cos\theta)}{\sin^2\theta}\right) \quad (1)$$

where B is the bending stiffness, Γ is the interfacial adhesion energy (126 mJ m^{-2} for graphene/*h*BN), θ is the bending angle, R is the radius of curvature, and H is the step height.[87] Note that this equation is based on the assumption of superlubricity at a misaligned graphene–*h*BN interface (to be discussed in section 4.3).

Through varying the step height of the *h*BN edges (H), the influence of the deformation condition was investigated (Fig. 2c and d). It was found that the experimentally measured B–N curves can be described by a power law dependence (Fig. 2e). Beyond a certain bending angle (>40°), the B–N curves exhibit a nearly linear relationship, characteristic of a stack of frictionless plates, indicating the onset of superlubricity between the graphene atomic layers (Fig. 2f). The reduced bending stiffness at high bending angles can be explained as a result of an increased contribution from an interlayer slip, which can accommodate the large strain at high angles (Fig. 2g).[87] It was also found that the bending stiffness of the graphene reaches a minimum when the thickness of the sample is reduced to a monolayer (Fig. 2e). Thus, the thickness of the 2D materials has an important impact on the flexibility of the sample that shall be discussed further in section 4.

3 Microscopy test methods

The size of single-crystal 2D materials is generally limited within a centimetre scale,[88–92] depending on the fabrication methods. Taking graphene as an example, the single crystal size is up to 500 μm when prepared by mechanical exfoliation,[91] or up to 1 cm size when synthesized by chemical vapour deposition (CVD).[14] Therefore, it requires microscopy techniques to reveal the intrinsic mechanical properties of 2D materials, such as nanoindentation experiments under AFM,[42,55,92,93] probe push tests under SEM/TEM, and tensile tests conducted based on a micro-electro-mechanical system (MEMS) under SEM/TEM.[51,94]

3.1 AFM nanoindentation

The AFM nanoindentation test has been widely applied to examine the intrinsic mechanical properties of 2D materials,[63]

Table 1 Comparison of the mechanical properties of 2D crystals as determined from experimental and from theoretical calculations, where L denotes layer, AFM denotes atomic force microscopy, SEM denotes scanning electron microscopy, TEM denotes transmission electron microscopy, MEMS denotes micro-electro-mechanical system, and DFT denotes density functional theory

Materials (fabrication methods)	Thickness	E^{2D} (N m^{-1})	Fracture strength σ_f (GPa)	E^{3D} (GPa)	Measurement methods	Ref.
Graphene (mechanical exfoliation)	1 L	340	130–110	1000	AFM nanoindentation	42
Graphene (mechanical exfoliation)	1 L	342 ± 8	125.0 ± 0	1026 ± 22	AFM nanoindentation	50
Graphene (mechanical exfoliation)	2 L	645 ± 16	107.7 ± 4.3	962.7 ± 23.9	AFM nanoindentation	50
Graphene (mechanical exfoliation)	3 L	985 ± 10	105.6 ± 6.0	980.1 ± 9.9	AFM nanoindentation	50
Graphene (mechanical exfoliation)	8 L	2525 ± 8	85.3 ± 5.4	942 ± 3	AFM nanoindentation	50
Graphene (CVD)	1 L	309	50–60	920	SEM MEMS tensile test	51
Graphene (mechanical exfoliation)	1 L	390		1147	Bulging test	52
*h*BN (mechanical exfoliation)	1 L	289	70	865	AFM nanoindentation	50
*h*BN (mechanical exfoliation)	2 L	590	68	881	AFM nanoindentation	50
*h*BN (mechanical exfoliation)	3 L	822	77	806	AFM nanoindentation	50
*h*BN (mechanical exfoliation)	9 L	2580	73.5	856	AFM nanoindentation	50
*h*BN (CVD)	1 L	200		601	SEM + TEM MEMS tensile test	53
*h*BN (CVD)	1 L	144.87	7.9	439	SEM MEMS tensile test	44
*h*BN (mechanical exfoliation)	10–70 L			770 ± 13	Bulging test	54
MoS_2 (mechanical exfoliation)	1 L	180 ± 60	22 ± 4	270 ± 100	AFM nanoindentation	55
MoS_2 (mechanical exfoliation)	2 L	260 ± 70	21 ± 6	200 ± 60	AFM nanoindentation	55
MoS_2 (CVD)	1 L	171.6 ± 12		264 ± 18	AFM nanoindentation	56
MoS_2 (CVD, mechanical exfoliation)	1 L	190 ± 35		283.6 ± 52.2	Bulging test	57
MoS_2 (mechanical exfoliation)	10–70 L			314.3 ± 8.4	Bulging test	54
MoS_2 (mechanical exfoliation)	3–11 L			246 ± 35	Surface wrinkling	58
MoS_2 (mechanical exfoliation)	1 L	172		265 ± 13	AFM	59
2H-$MoTe_2$ (mechanical exfoliation)	3.6 nm	316	5.6 ± 1.3	110 ± 16	AFM nanoindentation	49
2H-$MoTe_2$ (mechanical exfoliation)	6–6.7 nm	670 ± 5	5.6 ± 1.3	110 ± 16	AFM nanoindentation	49
1T′-$MoTe_2$ (mechanical exfoliation)	9–11 nm	1010 ± 60	2.6 ± 0.2	99 ± 15	AFM nanoindentation	49
T_d-$MoTe_2$ (mechanical exfoliation)	10.5–14 nm	1200 ± 100	2.5 ± 0.9	102 ± 16	AFM nanoindentation	49
$MoSe_2$ (CVD)	1 L	124 ± 6.5	3 ± 1	177.2 ± 9.3	SEM MEMS tensile test	60
$MoSe_2$ (CVD)	2 L	248 ± 13	6 ± 3	177.2 ± 9.3	SEM MEMS tensile test	60
2H-$MoSe_2$ (mechanical exfoliation)	2 L	157.38		122 ± 3	Brillouin light scattering	61
$MoSe_2$ (physical vapor transport)	5–10 L			224 ± 41	Surface wrinkling	58
$MoSe_2$	1 L		12–23	175–215	DFT	62
WSe_2 (mechanical exfoliation)	5 L	596	12.4	170.3 ± 6.7	AFM nanoindentation	63
WSe_2 (mechanical exfoliation)	6 L	690		166.3 ± 6.1	AFM nanoindentation	63
WSe_2 (mechanical exfoliation)	12 L	1411		167.9 ± 7.2	AFM nanoindentation	63
WSe_2 (mechanical exfoliation)	14 L	1615		164.8 ± 5.7	AFM nanoindentation	63
WSe_2 (mechanical exfoliation)	1 L	168 ± 25	38 ± 6	258.6 ± 38.3	AFM nanoindentation	64
WSe_2 (mechanical exfoliation)	3 L	489 ± 63	36 ± 5	238.9 ± 29.4	AFM nanoindentation	64
WSe_2 (mechanical exfoliation)	4–9 L			163 ± 39	Surface wrinkling	58
WS_2 (mechanical exfoliation)	1 L	187.5± 14.9	47± 8.6	302.4± 24.1	AFM nanoindentation	64
WS_2 (mechanical exfoliation)	3 L	489.4 ± 62.7	40.9 ± 6.0	263.1 ± 33.7	AFM nanoindentation	64
WS_2 (CVD)	1 L	177		272	AFM nanoindentation	56
WS_2 (mechanical exfoliation)	3–8 L			236 ± 65	Surface wrinkling	58
WTe_2 (mechanical exfoliation)	1 L	106 ± 6.6	6.4 ± 3.3	149.1 ± 9.4	AFM nanoindentation	64
WTe_2 (mechanical exfoliation)	3 L	272 ± 38		127.7 ± 18.1	AFM nanoindentation	64
WTe_2	1 L		14 ± 5	135–150	DFT	62
WN (CVD)	3 nm	764		260	AFM nanoindentation	65
WN (CVD)	4.5 nm	1804		400	AFM nanoindentation	65
WN (CVD)	12 nm	4490		370	AFM nanoindentation	65
HfS_2 (mechanical exfoliation)	12.2 nm	553	5.8 ± 0.4	45.3 ± 3.7	AFM nanoindentation	66
HfS_2 (mechanical exfoliation)	14 nm	1263	9.4 ± 0.3	90.2 ± 10.2	AFM nanoindentation	66

Table 1 *(Contd.)*

Materials (fabrication methods)	Thickness	E^{2D} (N m^{-1})	Fracture strength σ_f (GPa)	E^{3D} (GPa)	Measurement methods	Ref.
$HfSe_2$ (mechanical exfoliation)	13.4 nm	526	4.6 ± 1.4	39.3 ± 8.9	AFM nanoindentation	66
$HfSe_2$ (mechanical exfoliation)	15.4 nm	370	2.4 ± 0.1	24.1 ± 8	AFM nanoindentation	66
VS_2 (CVD)	9.2 nm	409	4.6 ± 0.2	44.4 ± 3.5	AFM nanoindentation	67
InSe (mechanical exfoliation)	6 L	528 ± 64		110 ± 13.4	AFM nanoindentation	68
InSe (mechanical exfoliation)	7 L	582 ± 125		104 ± 22.3	AFM nanoindentation	68
InSe (mechanical exfoliation)	8 L	646 ± 129	8.68	101 ± 20.0	AFM nanoindentation	68
InSe (mechanical exfoliation)	9 L	710 ± 118		99 ± 16.4	AFM nanoindentation	68
InSe (mechanical exfoliation)	14 L	1068 ± 202		95 ± 18.0	AFM nanoindentation	68
GaS (liquid exfoliation)	10 nm	1732	8	173	AFM nanoindentation	69
GaSe (liquid exfoliation)	10 nm	819	4	82	AFM nanoindentation	69
GaTe (mechanical exfoliation)	10 nm	246	2	25	AFM nanoindentation	69
Bi_2Te_3 (CVD)	10 L	187 ± 70	0.40 ± 0.08	18.7 ± 7	AFM nanoindentation	70
Bi_2Se_3 (CVD)	7–12 L			21.66 ± 3.8	AFM nanoindentation	71
Black phosphorus (mechanical exfoliation)	14.3 nm		25	276 ± 32.4	AFM nanoindentation	72
Black phosphorous (mechanical exfoliation)	11 L	110		106.6	AFM nanoindentation	73
Black phosphorus (mechanical exfoliation)	30–34 nm			89.7 ± 26.4	AFM nanoindentation	72
$Ti_3C_2T_x$ (liquid exfoliation)	1 L	326 ± 29	17.3 ± 1.6	333 ± 30	AFM nanoindentation	74
$Ti_3C_2T_x$ (liquid exfoliation)	1 L	473.9	15.4	484 ± 13	SEM MEMS tensile test	34
$Nb_4C_3T_x$ (liquid exfoliation)	1.26 nm	486 ± 18	26 ± 1.6	386 ± 13	AFM nanoindentation	75
Mica (mechanical exfoliation)	2–14 L		4–9	202 ± 22	AFM nanoindentation	76
$COF_{TTA\text{-}DHTA}$ (confined synthesis)	4.7 nm	119 ± 3		25.9 ± 0.6	AFM nanoindentation	77
COF (confined synthesis)	44 ± 7 nm polycrystalline film	2494 ± 325	1.86 ± 0.2	56.7 ± 7.4	AFM nanoindentation	29
MOF(CuBDC) (liquid exfoliation)	10 nm	230		23	AFM nanoindentation	78
Perovskite(C_4n_3) (mechanical exfoliation)	1 L	29.4 ± 3.6	0.7 ± 0.08	11.2 ± 1.4	AFM nanoindentation	79
Perovskite(C_4n_3) (mechanical exfoliation)	2 L	37.1 ± 4.9	0.44	7.1 ± 0.9	AFM nanoindentation	79
Perovskite(C_4n_3) (mechanical exfoliation)	3 L	43	0.36	5.7	AFM nanoindentation	79
Perovskite(C_4n_3) (mechanical exfoliation)	4 L	60	0.36	5.7	AFM nanoindentation	79
Bi_2O_2Se (CVD)	5 L	307	18–23	88.7 ± 14.4	AFM nanoindentation	80
Bi_2O_2Se (CVD)	10 L	507	18–23	88.7 ± 14.4	AFM nanoindentation	80
Bi_2O_2Se (CVD)	15 L	768	18–23	88.7 ± 14.4	AFM nanoindentation	80
$Cr_2Ge_2Te_6$ (mechanical exfoliation)	14 L	515		56.2 ± 8.2	AFM nanoindentation	81
$Cr_2Ge_2Te_6$ (mechanical exfoliation)	20 L	770		55	AFM nanoindentation	81
$Cr_2Ge_2Te_6$ (mechanical exfoliation)	34 L	1240		53	AFM nanoindentation	81
$Cr_2Ge_2Te_6$ (mechanical exfoliation)	42 L	2000		70	AFM nanoindentation	81
$CrCl_3$ (mechanical exfoliation)	2 L	106	3.6 ± 0.4	62.1 ± 4.8	AFM nanoindentation	82
$CrCl_3$ (mechanical exfoliation)	10 L	230	2.2 ± 0.2	27.1 ± 2.5	AFM nanoindentation	82
CrI_3 (mechanical exfoliation)	2 L	61	2.2 ± 0.5	43.4 ± 4.4	AFM nanoindentation	82
CrI_3 (mechanical exfoliation)	9 L	100	1.6 ± 0.04	15.8 ± 1.2	AFM nanoindentation	82
$TaNi_2Se_5$ (mechanical exfoliation)	28 nm		2.4 ± 0.8 for *a* axis, 1.2 ± 0.2for *c* axis	56.9 ± 9.2 for *a* axis, 45.0 ± 4.5 for *c* axis	SEM MEMS tensile test	28
As_2S_3 (mechanical exfoliation)	9–25 nm			79.1 ± 10.1 for *a* axis, 47.2 ± 7.9 for *c* axis	AFM nanoindentation	83

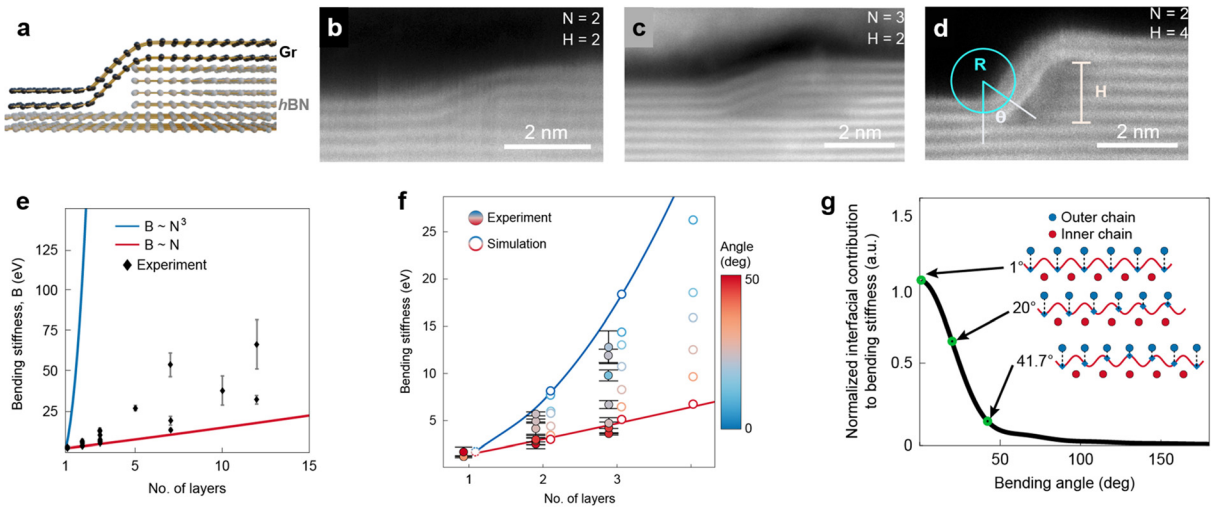

Fig. 2 Measuring bending stiffness through imaging the geometry of curved 2D materials. (a) Schematic showing the heterostructure used for measuring the bending stiffness of graphene. Bilayer graphene was transferred onto the top of an *h*BN edge step.[87] (b–d) Annular dark-field scanning transmission electron microscopy (ADF-STEM) images showing the cross-sectional samples prepared from *N*-layer graphene samples over *H*-layer *h*BN steps. For each designed *N* and *H*, a bending profile was measured containing a radius of curvature *R*, step height *H* and bending angle *θ*, indicated in d.[87] (e) Plots showing the bending stiffness measured as a function of the thickness of graphene from experiments. Power law relationships are denoted by the red and blue lines just for comparison.[87] (f) The experimentally measured (filled symbols) and calculated (open symbols) bending stiffnesses as a function of thickness for few-layer graphene. The blue and red colouring is to show the various bending angles where the data are measured from.[87] (g) Calculated contribution to bending stiffness from interfacial interaction, as a function of bending angle, based on simplified Frenkel–Kontorova model. The inset shows that the curvature is accommodated entirely by slip between the layers. Reproduced from ref. 87 with permissions from Springer Nature Limited Copyright 2019.[87]

as well as effects from defects[95] and grain boundaries.[92] For a typical indentation test set-up, 2D materials were transferred onto a holey substrate (*e.g.* SiO_2/Si) with micro-sized wells. Outside the wells, the continuous graphene membrane is firmly fixed through van der Waals (vdW) attraction to the substrate.[96] Inside those wells, 2D materials are suspended as a membrane, where the indentation tests are conducted until fracture happens. From the experiments, the curves of applied force–indentation depth can be directly measured, and most 2D materials show a brittle fracture behaviour. By fitting those curves, E^{2D} can be deduced by the non-linear Föppl membrane theory. Namely,

$$F = \sigma_0^{2D}(\pi a)\left(\frac{\delta}{a}\right) + E^{2D}(q^3 a)\left(\frac{\delta}{a}\right)^3 \quad (2)$$

in which F is the applied force, σ_0^{2D} is the membrane pretension, δ is the deflection depth at the centre point, a is the radius of the membrane, E^{2D} is the two-dimensional Young's modulus, and $q = 1/(1.049–0.15\nu–0.16\nu^2)$.[42]

The failure mechanism of 2D materials in response to cyclic and impact loading has been a recent research interest. Fatigue behaviour and damage mechanisms are critical to evaluating the long-term reliability of devices made from 2D materials, because fatigue can cause material failure at stress levels significantly lower than that under static loading. A modified AFM instrument was developed recently to enable applications of both static and cyclic loading to suspended 2D materials. Through adding alternating current inputs using a 'shake' piezo (Fig. 3a–c), Cui *et al.* conducted a fatigue test on graphene and found that it exhibits a fatigue life of more than 10^9 cycles under a mean stress of 71 GPa, higher than any material reported so far.[32] Unlike metals, there is no progressive damage during the fatigue loading of graphene, and its failure is global and catastrophic (see bottom inserts, Fig. 3b). Furthermore, this study illustrates the difference between the morphological changes of bilayer and monolayer graphene during fatigue. Bilayer samples exhibit obvious interlayer shearing and wrinkling after failure, whereas no such behaviour was observed for monolayers after one billion cyclic loadings (Fig. 3c and d). The fatigue behaviour of graphene and graphene oxide (GO) was also compared. In contrast to the catastrophic failure behaviour in graphene, monolayer GO films exhibited localized failure. This could be attributed to the enriched oxygen functional groups in graphene oxide, where epoxide-to-ether transformation can happen during stress loading, which provides trapping sites for cracking arresting, leading to the occurrence of unusual plasticity in graphene oxide.

However, nanoindentation tests have their own limitations. For example, they can only measure a small sample area underneath the indenter tip (tip radii < 50 nm), which does not necessarily represent the properties for the whole membrane.[97–99] Also, nanoindentation cannot directly measure fracture strength σ^{2D}. It gives an estimated value of inferred from E^{2D} and δ, using theoretical stress–strain relationships, *e.g.* $\sigma^{2D} = \left(\frac{FE^{2D}}{4\pi R}\right)^{\frac{1}{2}}$ with R being the indenter

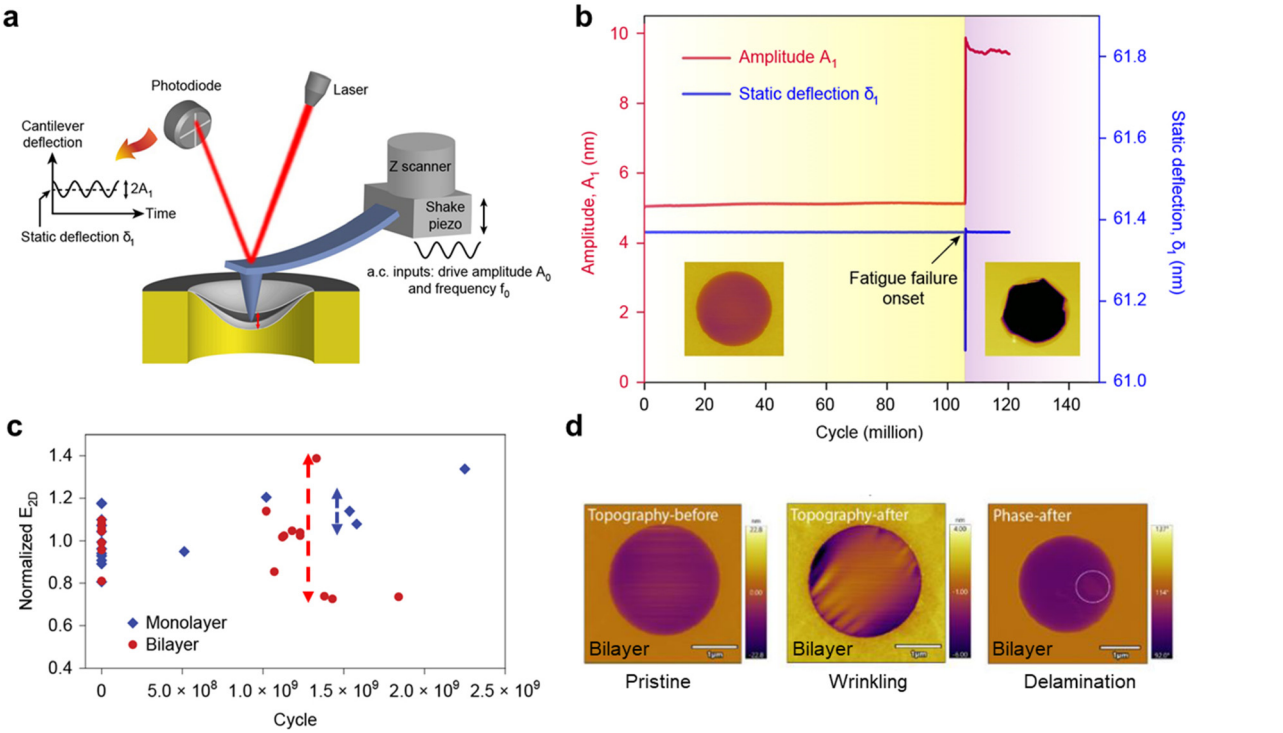

Fig. 3 Fatigue test conducted on free-standing graphene using AFM.[32] (a) A schematic illustrating the set-up for fatigue testing.[32] (b) A typical result from a fatigue test conducted on a bilayer graphene under a static loading with a value at half of its fracture force. The abrupt jump in the amplitude and deflection signals at ~100 million cycles indicate the occurrence of fatigue failure. The insets are AFM images taken before and after the fatigue failure. The diameter of the sample is 2.5 μm. In such a case, the maximum in-plane stress varies from 69.5 to 75.1 GPa calculated using DFT-based nonlinear FEM.[32] (c) Normalized elastic modulus E^{2D} of monolayer and bilayer graphene. E^{2D} values are normalized by that measured from the pristine samples without fatigue loading. The red and blue dashed lines are guides to the eye for showing the larger scatter in the E^{2D} for the bilayer compared with monolayer.[32] (d) Corresponding cyclic loading-induced wrinkling and local delamination, while no morphological change was observed for the monolayer after cyclic loading. Reproduced from ref. 32 with permissions from Springer Nature Limited Copyright 2020.[32]

tip radius, assuming a clamped, linear elastic, circular membrane, or $\sigma \sim \delta$ curves that requires combination with theoretical predictions from density functional theory (DFT) and finite elemental analysis (FEM).[32]

3.2 *In situ* probe SEM/TEM bending tests

In the recent two decades, the probe measurements conducted under SEM and TEM, through using *in situ* pushing set-ups like AFM–TEM and the STM–TEM holders, have been widely used, in particular for understanding the bending behaviour of one-dimensional and three-dimensional samples. For 2D metal chalcogenides, *in situ* probe tests have been mostly conducted on their bulk counterparts, such as MoS_2 and InSe single crystals. For example, combining the experiments with high-throughput calculation, Shi *et al.* revealed tens of potential 2D metal chalcogenide crystals with plastic deformability, as shown in Fig. 4. Such plasticity is unexpected, as most vdW semiconductors are believed to be brittle because of their weak interlayer forces. Fig. 4c shows a stress–strain curve of InSe taken by SEM compression tests, clearly showing slip-induced strain bursts, similar to those of metals.[26] The interlayer slipping energy barrier of InSe is as low as 0.058 eV per atom. In contrast, the cleavage energy is as high as 0.084 eV, such that the constituent layers can maintain integrity during slip, making plastic deformation possible.[26]

The *in situ* probe test can also be used to illustrate the detailed structural evolution process of the 2D metal chalcogenides during deformation, through utilizing the resolution advantages of TEM imaging, *i.e.* high temporary and spatial resolution. Recently, Zhao *et al.* directly observed the atomic-scale plasticity mechanism in 2D InSe flakes using an *in situ* TEM bending test (Fig. 5), with complementary high-resolution STEM imaging.[30] It was interesting to see that a phase transition from 2H to 3R occurred in InSe crystals during the deformation (Fig. 5a–c). The *in situ* characterization studies found that InSe exhibits an unusual plastic deformability, where not only do the interlayer gliding and formation of high-density dislocation networks play a role, but the appearance of numerous discontinuous nanoscale cracks also has an impact, which helps release the increased local elastic energy due to deformation (Fig. 5d–i). Such behaviour distinguishes InSe from other materials such as MoS_2, and $MoTe_2$, where large cracks across the whole crystal were observed.[30] To illustrate the different deformation behaviour between the materials, further DFT calculations were conducted and indicated that the bonding strength of In–Se (3.855 eV per bond) is

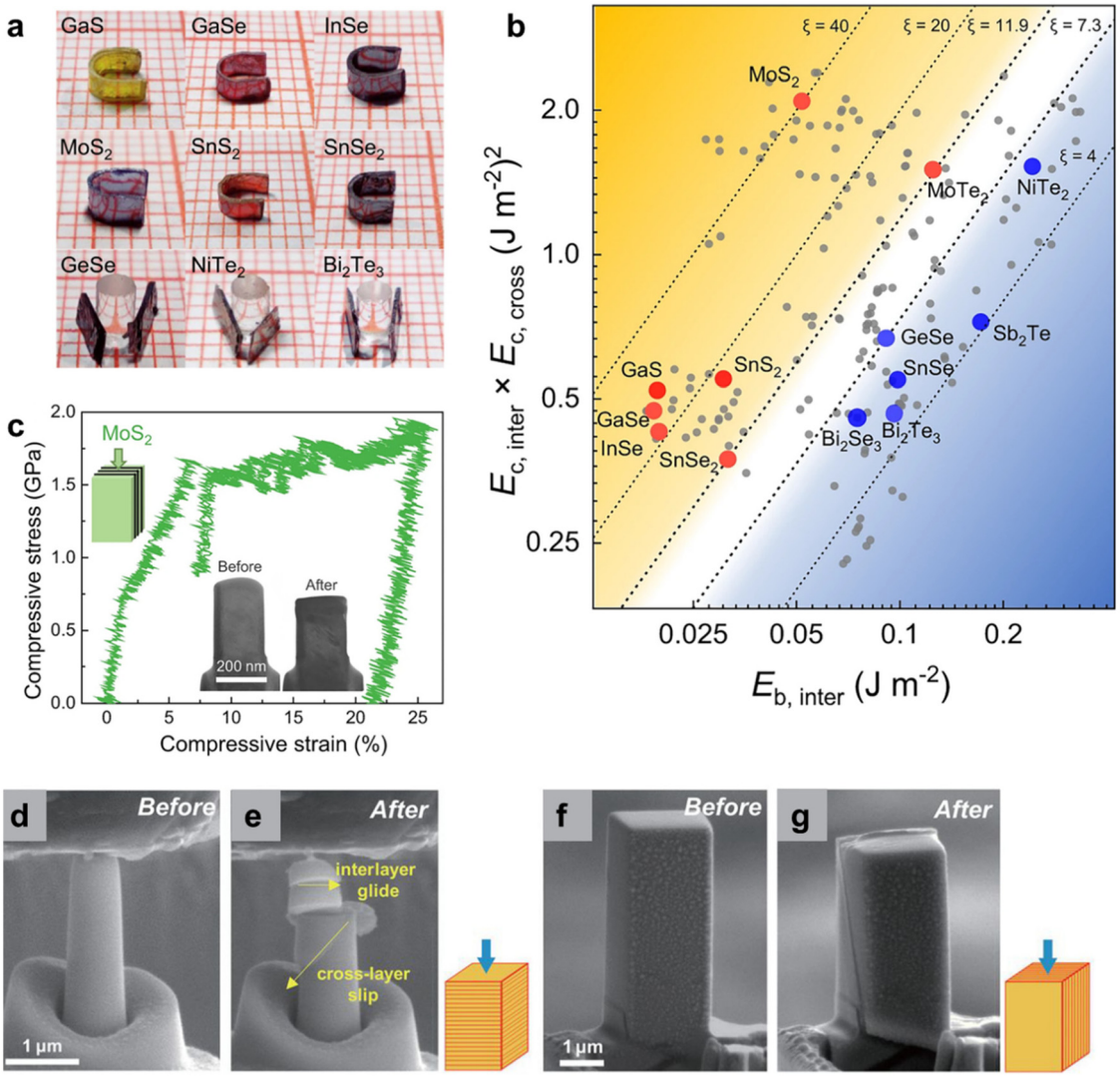

Fig. 4 (a) Digital photos of the bent metal chalcogenide samples. The smallest grid is 1 mm.[39] (b) A combined index ξ, $(E_{c,inter} \times E_{c,cross})/E_{b,inter}$ to predict 2D vdW materials with plasticity. A plastically deformable 2D vdW crystal should possess a large ξ.[39] (c) *In situ* TEM compression test results, with the top showing stress–strain curves taken from a small micro-machined MoS_2 pillar and the bottom part showing TEM images taken before and after the test.[39] (d–g) SEM images taken from an *in situ* SEM compression test on InSe micropillars along (d and e) and perpendicular (f and g) to the (001) axis. Reproduced from ref. 26 with permissions from The American Association for the Advancement of Science Copyright 2020.[26]

weaker than Mo–S (4.368 eV per bond). Therefore, it is relatively easier to break the intralayer In–Se bond, so that the occurrence of cracks is energetically permitted.[30] DFT results also explained how phase transition initiates during the deformation of InSe, which suggests that the transition from 2H to 3R in InSe is more energetically favourable compared with those phase transitions in other materials systems such as MoS_2 and $MoTe_2$. The above work demonstrates the important role of *in situ* TEM tests in mechanistic studies for deformation.[30]

However, the application of *in situ* probe tests for 2D samples is still limited, especially for those atomically-thin ones. The mechanical loading onto a sample is based on a tip with nanometre-scale contact size (see Fig. 5), which is much smaller than the lateral size of most 2D samples while much larger than their thickness, leading to a deformation geometry limited to quasi-1D nanoscrolls. It is therefore remotely possible to use this approach to achieve a controllable and even stress loading, or a quantitative understanding of mechanics in 2D materials. This necessitates the development in micro-electro-mechanical system (MEMS) devices for quantitative experiments, which shall be discussed in the following section.

3.3 Tensile test using MEMS in SEM and TEM

Tensile tests are the most fundamental method to directly measure the fracture strength of bulk materials.[94] However, for 2D materials, there are a limited number of research groups doing the *in situ* tensile tests, due to the technical challenges in the micro-scale sample handling process. The MEMS specific for conducting tensile tests on 2D materials has devel-

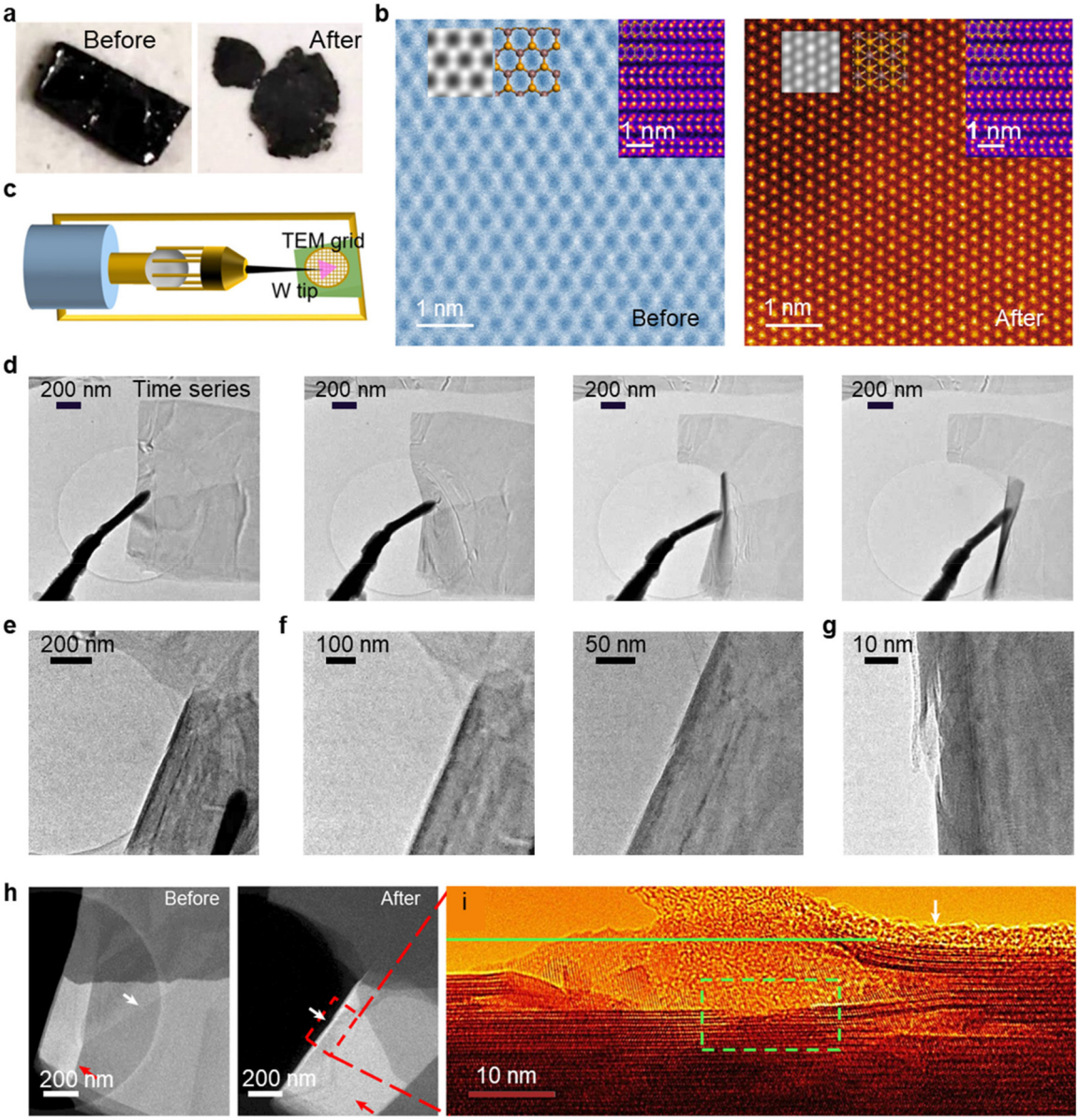

Fig. 5 (a) Digital photos taken from a InSe crystal, before (left panel) and after (right panel) the *ex situ* compression test.[30] (b) High-angle angular dark field-scanning transmission electron microscopy (HAADF-STEM) images taken from InSe crystals, before (left panel) and after (right panel) the *ex situ* compression test, showing the pristine sample has a 2H phase, while the compressed sample has a 3R phase.[30] (c) Schematic showing the experimental set up for the *in situ* TEM deformation tests. Reproduced from ref. 100 with permissions from The American Association for the Advancement of Science Copyright 2022.[100] (d–g) Time-series TEM snapshots, selected from the recorded video taken during the *in situ* bending experiment, which included TEM images taken before the fracture happens (d), with a corresponding magnified TEM image (e and f) and a rotated and high-resolution TEM image shown in g.[30] (h) Corresponding HAADF-STEM images taken before (left panel) and after the *in situ* experiment.[30] (i) Corresponding high-resolution TEM image. The fracture and nanoscale cracks formed at the edge of the sample were marked by a green line and a green box respectively. Reproduced from ref. 30 with permissions from Springer Nature Limited Copyright 2024.[30]

oped significantly within the recent few years. Such *in situ* tensile instruments mainly contain a push-to-pull (PTP) micromechanical platform,[101] where a push from a pico-indenter generates the force to pull the two ends of a micro-sized 2D sample (Fig. 6). Unlike the nanoindentation tests described in the previous section, MEMS tests apply a uniform uniaxial stress onto the sample and thus enable quantitative measurements of mechanical properties. However, the MEMS-based tests require comparatively complex sample transfer procedures, including the isolation and transfer of suspended 2D materials, and sample shaping using techniques like the focused ion beam (FIB), as illustrated in Fig. 6. The MEMS device is quite similar to other types of suspended 2D device, *e.g.* acoustic devices, and so are the transfer methods.[102] Transfer methods of 2D materials can be classified as wet transfer and dry transfer. Choosing which method is depend-

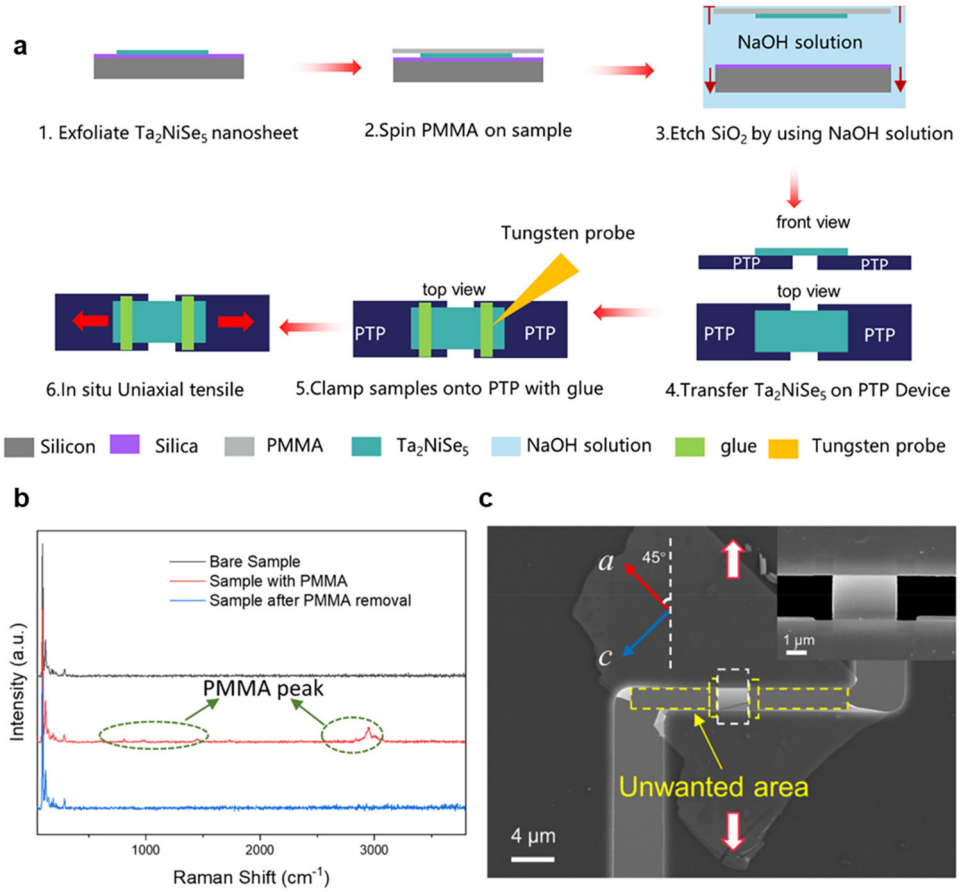

Fig. 6 A schematic showing the typical transfer process for 2D materials samples onto MEMS chips, composed of three steps. (a) The polymer-assisted transfer process onto MEMS chips.[28] (b) Removal of the polymer after transfer, confirmed by Raman spectroscopy.[28] (c) The clamping and shaping of sample under FIB.[28]

ing on the original substrate of the source 2D materials. Wet transfer is suitable for most source materials regardless of their adhesion to the substrate, as it directly removes or dissolves the original substrate so that the materials can be suspended over a solution. For example, the widely used etchants for dissolving substrates are $FeCl_3$ for copper-supported CVD graphene and KOH for SiO_x-supported graphene.[103] This suggests both sides of the 2D materials contact and contaminated with a considerable amount of solution, which is not ideal if the purpose is to measure intrinsic mechanical properties by using clean samples. To obtain contamination-free samples, dry transfer has been a major research direction. The dry transfer results in only one side of the 2D materials' surface being in contact with the solutions or carrying layers, so that the other surface remains intact and clean. Dry transfer is achieved through two approaches: one is adding a water-soluble sacrificing layer, *e.g.* the widely used a composite layer made by stacking polyvinyl alcohol (PVA) on polymethyl methacrylate (PMMA), and the other is using the 'dry-stamp' method, which only applies to those materials that are not strongly adherent to the original substrate *e.g.* mechanically exfoliated ones. The dry stamp is conducted by removing and transferring the 2D materials from the original substrate to the target substrate, using a carrier layer mostly composed of polymers like poly-dimethylsiloxane (PDMS) and PMMA.[104] To further improve the sample cleanliness, a polymer-free transfer would be ideal, for which the composition of the carrying layer has to be changed to non-polymer ones, *e.g.* metal and ultra-flat SiN_x membranes with improved adhesion to the 2D materials.[104] However, the dry-stamp methods have rarely been applied to the mechanical test devices of 2D materials, since the stamping force might destroy the MEMS chips, which are mechanically fragile due to the cavity structures. Also, the adhesion between the 2D materials and the MEMS device can be smaller compared with the adhesion to the carrying layer, which makes the success rate of transfer limited. Therefore, it is still challenging to apply dry transfer in the fabrication of MEMS devices[105] with contamination-free 2D materials. Nevertheless, through using MEMS in combination with the advances in electron microscopy instruments, quantitative tensile tests have been conducted in a few types of 2D material under TEM and SEM, including *h*BN,[44] graphene,[94] TMDs,[60,106] transition metal nitrides and carbides,[34] and covalent organic frameworks (COFs).[107]

The sample quality control is highly important for realizing a reliable and quantitative tensile test on 2D materials.[51] Fig. 7a shows a schematic of a shaped graphene flake on a tensile testing MEMS chip. By improving sample quality using a modified transfer method, Lu *et al.* measured a Young's modulus $E^{3D} \sim 900$–1000 GPa from a CVD-grown graphene, fairly close to the theoretical value of a pristine monolayer graphene.[51] This work approached an elastic strain limit of ~6% (Fig. 7b), higher than previously reported experimental values. It should be noted that this value ~6% is still lower compared with the theoretical strain limit of ~20%, with the representative tensile fracture strength of ~50–60 GPa measured as being smaller than the ideal strength of monolayer graphene (~100–130 GPa). This could result from the presence of defects when preparing shaped samples for tensile tests.[51] It is well-documented that point defects, line defects, pre-cracks at the

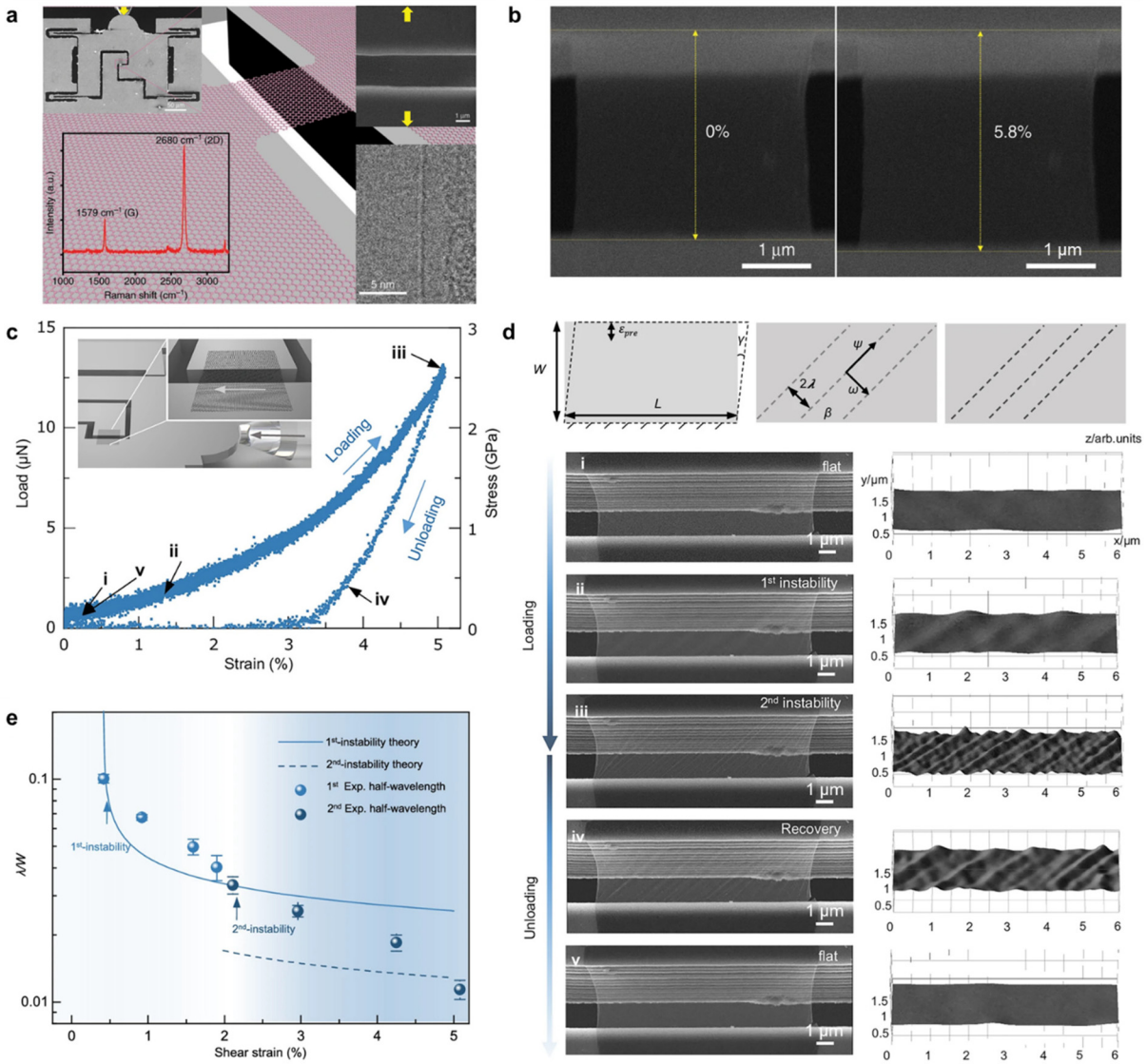

Fig. 7 Experimental *in situ* tensile techniques for measuring elastic properties. (a) Schematic showing a single-crystalline graphene sample suspended over the push-to-pull (PTP) micromechanical device. Left top is an SEM image showing an overview of the PTP device actuated by an external pico-indenter. Right top, zoom-in SEM image taken from the region marked by a rectangle in the left-top inset. The yellow arrows indicate the indentation or stress loading direction. Left-bottom inset showing a Raman spectrum taken from the graphene sample. Right-bottom inset showing a TEM bright-field image taken from the sample edge, where an amorphous edge can be observed.[51] (b) SEM images taken before and after an *in situ* tensile test conducted on the suspended graphene.[51] (c) Stress–strain curves recorded during the loading and unloading process, in which the arrows denote the emergences and disappearances of the instabilities. The inset is a schematic showing the push-to-shear experimental setup for introducing shearing strain into the 2D materials.[31] (d) Time-sequence SEM images taken from the *in situ* shear test conducted from the monolayer graphene, and the corresponding models describing the sample morphologies during deformation. The top inset is a schematic showing the geometrical parameters of the wrinkling structure.[31] (e) Curves present the theoretical normalized wrinkling wavelengths as a function of the shear strains during different stages of instability, in which the solid balls are experimental data points.[31]

sample edge or the sample clamping sites, and oxidized impurities, can be introduced simply due to sample preparation, which leads to considerably reduced strength in 2D materials.[32,51,92,94,108] The current shaping methods are generally based on FIB ion milling,[109] where ion implantation can lead to surface damage and edge defects in the specimen.[51] On the other hand, the transfer of 2D materials with an atomically-thin thickness, especially monolayers, is still challenging due to the low accessibility of the source materials, and the high adhesion of these samples to their original substrates. Very recently, Rong *et al.* developed a copper mesh-assisted transfer technique, which uses the thin flakes that attached locally to a mesh edge as the source materials.[34] The limited attaching area leads to limited adhesion to the substrates, therefore allowing the subsequent transfer of the flakes by FIB nanomanipulation.[34] This increases the accessibility to the intrinsic mechanics of monolayer samples. Therefore, to fully understand the fundamental factors that govern the intrinsic mechanical performance of 2D materials, there is much room for improving sample preparation and testing methods.

Meanwhile, there are tensile tests finding that flaw insensitivity exists in 2D materials.[53,107] Insensitivity to the pre-existing flaw, such as voids[53] and pre-cracks, was observed in *h*BN and 2D COF.[53,107] For example, Han *et al.* found that the maximum tensile strain of *h*BN monolayers reaches ~6%, even though some pre-existing voids were present in the testing samples.[53] They found that the naturally occurring voids are not detrimental to the mechanical resistance of *h*BN. Instead, those defects introduced by FIB to the sample clamped region and the sample edge are responsible for the maximum strain loss of the monolayer. This indicates that the contribution from defects depends on the specific type of the defect and the materials.

For applications especially in resonator and acoustic devices, it is important to know how the morphology and structure of the 2D materials evolve in real working conditions. Recently, a mechanical push-to-shear approach was developed to illustrate the dynamic wrinkling–splitting–smoothing process of suspended 2D materials (Fig. 7c–e). Shear stress–strain curves of single-layer graphene are shown in Fig. 7c, from which the in-plane shear modulus of the monolayer graphene was determined as ~70 GPa based on the initial linear stage, slightly larger than the previously measured result, possibly due to the initial corrugations in the sample.[110] As illustrated in Fig. 7c and d, during stress loading, the first appearance of wrinkling is marked as the 1st instability. As the shear strain increases beyond a certain threshold, wrinklons are observed with a reducing wavelength of the wrinkles, marked as the 2nd instability, where the wrinkling–splitting happens at a halving of the wavelength, while for the unloading process, the smoothing happens mainly as a result of the reduced amplitude instead of wavelength changing or merging of the wrinkles. Such a difference in stability between the formation and recovery processes can be explained by the redistribution of local compressive stain. The function between $D \sim f(E,\varepsilon_{Pre},\gamma)\lambda^4$ was also summarized for the initial instability stage, where D denotes the bending stiffness, E denotes the Young's modulus, ε_{pre} denotes the pre-tension strain applied on the film, γ denotes the strains, and λ denotes the observed wrinkling wavelength (Fig. 7d and e). The wrinkling wavelength possesses positive correlations with bending stiffness and pre-tension and a negative correlation with Young's modulus and shear strain. Thus, the MEMS *in situ* tensile test provides a direct pathway to observe and understand the wrinkling behaviour of suspended 2D materials under dynamic stress loading.[31]

Compared with other *in situ* methods, the tensile test under TEM has such advantages that it combines the sub-angstrom spatial resolution imaging capability of TEM during the experiments. Fig. 8 shows such a case study conducted by Zhang *et al.*, where the atomic structure at the crack edge was characterized using HRTEM, in combination with the *in situ* SEM tensile test. It was revealed that the Young's modulus and fracture strength of 2D Ta_2NiSe_5 (TNS) along the *a*-axis were measured to be 56.9 ± 9.2 GPa and 2.4 ± 0.8 GPa, respectively, both higher than those along the *c*-axis (45.0 ± 4.5 GPa and 1.2 ± 0.2 GPa). The correlated high-resolution TEM imaging confirms the crack paths of 2D TNS along different orientations. As shown in Fig. 8a and c, for a TNS sample stretched along the *a*-axis, the crack edge is sharply formed at an angle of 30° related to the *c*-axis, and a similar crack structure was observed from the other samples subjected to a 45° counterclockwise rotation (Fig. 8e). In contrast, when the loading direction is parallel to the *c*-axis (Fig. 8d), a straight crack with an angle of 90° is observed, confirmed by the atomic resolution imaging using TEM. The high-resolution imaging confirms the accuracy of the atomic models used by the subsequent DFT calculation, so that the energetic reasons behind the observed cracking behaviour can be well explained (Fig. 8f).

Despite the as-mentioned developments, there remain few concerns regarding the accuracies of the above microscopy methods, which are often related to sample preparations and displacement measurements. Take the widely used AFM method as an example; since the cantilever is perpendicular to the basal plane of the 2D materials, the atomic layer that contacts the AFM probe may deviate and slip from the normally aligned atomic structure, resulting in a serious mis-arrangement of the atoms and inhomogeneity in the stress field.[34] The other controversy still lies in the uncertainty of the sample quality, *i.e.* the crystal defects and the contamination introduced during sample preparation, *e.g.* the polymer adsorbent from polymer-assisted 2D sample transfer, the Pt contamination and Ga ion implantation during Pt deposition in the FIB, and the amorphization and artificial cracking due to ion beam damage on 2D samples in the FIB. On the other hand, the data processing for quantitative measurement needs extra care. For instance, the sample thickness is difficult to precisely measure, either on the SiN_x membrane device used for AFM nanoindentation, or on the MEMS chips for electron microscopy. These inaccuracies can arise from the contamination added on the top of the sample surface, or simply due to the fact that the substrate has limited flatness, where ang-

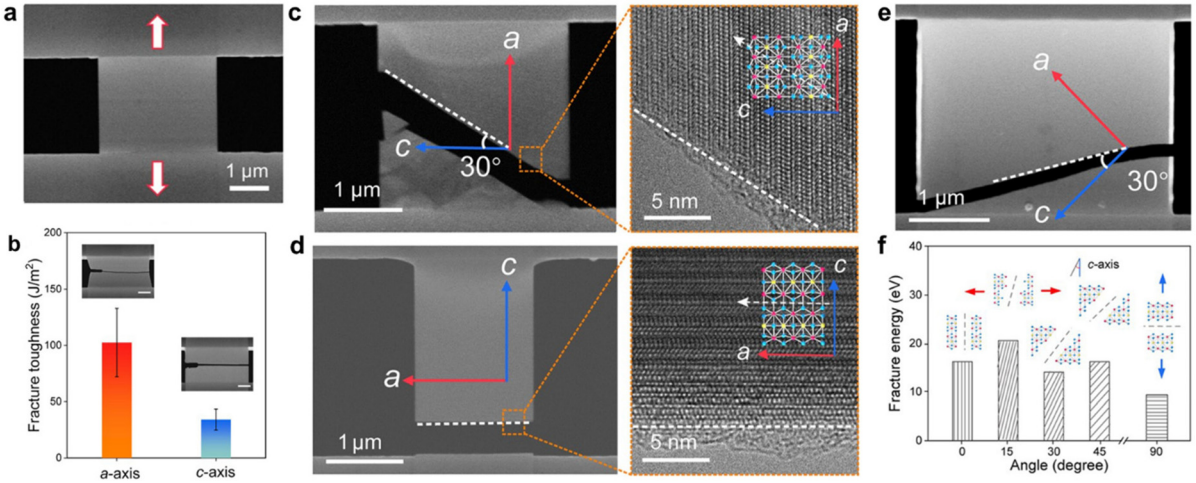

Fig. 8 Tensile test conducted on an anisotropic 2D Ta_2NiSe_5 crystal. (a) An overview SEM image showing Ta_2NiSe_5 membrane on a "Push-to-Pull" MEMS device.[28] (b) Measurements of anisotropic fracture toughness for different samples. Scale bar: 1 μm.[28] (c) SEM image taken from a cracked *a*-axis sample, and a corresponding HRTEM image taken from the crack edge.[28] (d) SEM image taken from a cracked sample with its long axis being the *c*-axis and the corresponding HRTEM image taken from the crack edge.[28] (e) SEM image taken from a cracked sample with its axis being 45° to the *c*-axis.[28] (f) DFT calculated fracture toughness using samples cut with various angles to the *c*-axis direction. Reproduced from ref. 28 with permissions from American Chemical Society Copyright 2024.[28]

strom-scale inaccuracies can lead to errors when determining the number of atomic layers in the sample. Also, the sample thickness may change before and after the test, and therefore nominal thickness, calculated from an assumed number of atomic layers based on the measurement before testing, is often used, leading to inaccuracies in the calculation of E^{3D}. Besides, the imaging quality during tests is influencing the accuracy of the final results. Take the *in situ* MEMS SEM/TEM test as an example; the elastic strain of most 2D materials is within 10%, which means the deformation is on a nanometre scale. However, the recording of the *in situ* test requires a low magnification imaging for the whole sample area. This causes a limitation in pixel resolution and may not satisfy the accuracy required for the measuring the elastic deformation. Therefore, improvements in measurements are still required, especially on sample preparation and imaging techniques such as polymer-free sample transfer[104] and correlated imaging.[30,38,111]

4 Effects of structure

4.1 Thickness

Failure mechanism under tensile stress. For monolayer specimens (Fig. 9a), fracture failure is triggered by critical bond breakages in strained atomic rings,[112] originating from the defects that are intrinsic or introduced by sample preparation, or developed during deformation, *e.g.* vacancies[32] and Stone–Thrower–Wales defects.[113] Note that the bonding stretching and breaking process varies with the type of material, as demonstrated in previous sections. Within the same material, such a process can be anisotropic, which changes with the force loading direction, for example the zigzag or armchair crystallographic directions in hexagonal structure materials,[114] as mentioned in Table 1 and shown in Fig. 8. For few-layer and multi-layer specimens, the interlayer interaction plays an important role during the deformation process,[50,52] with an increased importance with an increasing number of layers, where interlayer shearing caused stacking faults, local wrinkling and delamination (Fig. 9). In a deformation process in a multi-layer sample, the local shear deformation accumulated from an external applied force would eventually overcome the energy barrier for the adjacent layers gliding to find their next stable state (*i.e.* another favourable interlayer registry). For example, such a deformation behaviour was observed in a trilayer graphene embedded in polymer.[115] Application of tensile strains to the top and bottom atomic layers changes the balance of the elastic and interlayer interaction energies. Upon increasing the strain, it becomes favourable to release the excessive elastic energy by the formation of dislocations. The density of dislocations increases upon continuously increasing the strain above a certain critical value, and the second-order phase transition from the commensurate to incommensurate phase occurs, characterized by a high density of dislocations and stacking faults.[116] This further initiates interlayer and intralayer slippage, leading to atomic bonding breaks and the final delamination.[117]

Failure mechanism under bending. Compared with tensile stretching, it is more difficult to cause the fracture by bending in thin 2D materials, since thin 2D materials should be highly bendable with an incommensurate interlayer registry achievable under high curvatures, in analogy to their nanotube's form, *e.g.* carbon nanotubes and MoS_2 nanotubes (Fig. 10). For multilayer specimens, the deformation and fracture mechanisms are more complex, which depends on the external force conditions, *e.g.* the loading application methods,[45,86,87] and

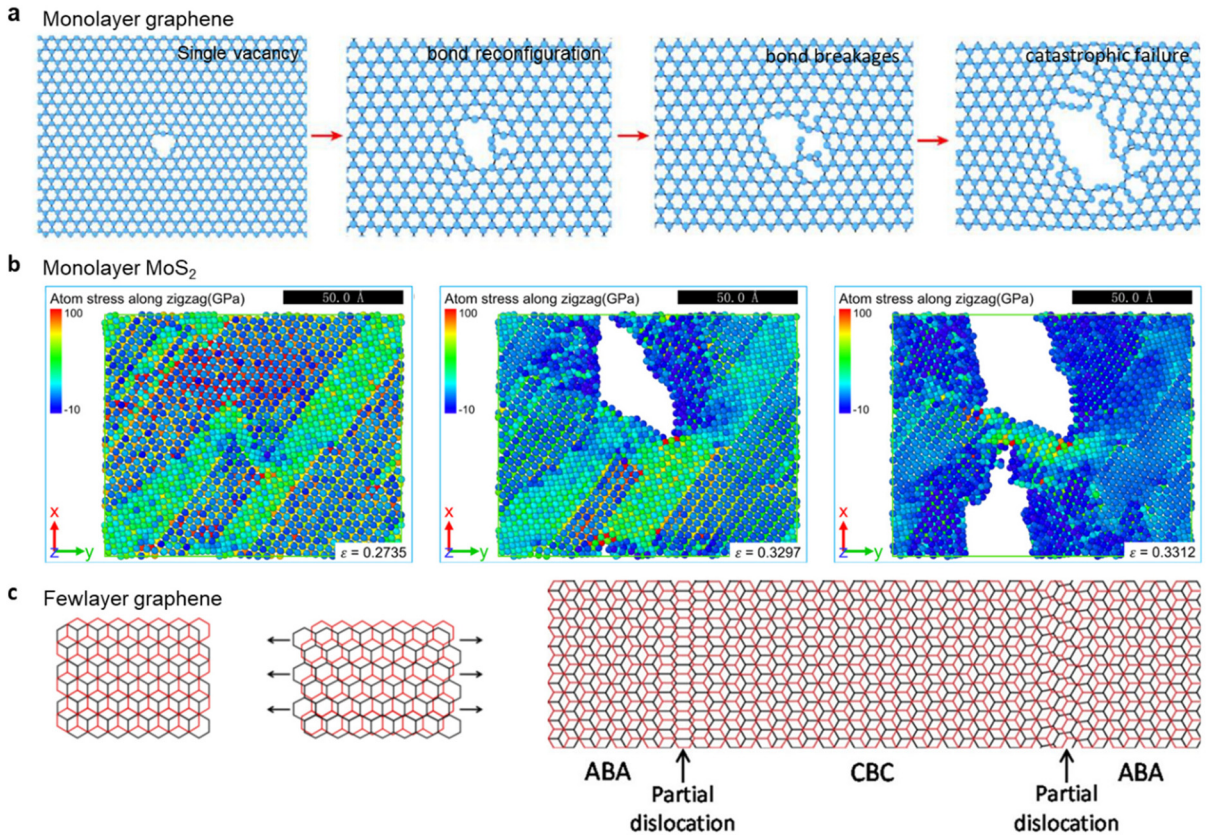

Fig. 9 Fracture and deformation mechanisms under tensile stress. (a) Molecular dynamics (MD) modelling of the failure process of a monolayer graphene with a single-vacancy defect, under a strain rate of 10^9 s^{-1}, showing bond-stretching failure mode.[32] (b) MD modelling of the uniaxial tensile fracture processes of a monolayer MoS_2 under a strain rate of 10^9 s^{-1}, loading along zig zag directions, with the left panel showing the result from elastic strain ε = 0.2735, the middle panel showing ε = 0.3297, and the right panel showing ε = 0.3312. Reproduced from ref. 120 with permissions from IOP Publishing Ltd Copyright 2020.[120] (c) Schematic illustration of atomic structure evolution during shear deformation of trilayer graphene, with left panel: initial ABA Bernal structure; middle panel: deformed structure with a rigid lattice with the shear process taking place at the top and bottom layers; right panel: relaxed deformation structure, with the formation of partial dislocations as a result of the low stacking fault energy.[115]

the bending angle.[118] The process involves the formation of kink bands[119] and twinning (Fig. 10c), which are weak points for oxygen attack and local delamination (Fig. 10d), followed by edge peeling and fracture failure.[45,86,87,111]

4.2 Defects and grain boundaries

The strength and stretchability of 2D materials are limited by the presence of point and line defects,[97,122,123] pre-existing cracks or voids[99,111,124] and impurities at the grain boundaries (GBs). Point defects in 2D materials include vacancies where an atom is missing (Fig. 11a), impurities where foreign atoms reside in a substitutional or interstitial site,[125] and paired point defects that occurred solely due to local bonding rotation and reconfiguration, such as Stone–Thrower–Wales defects (Fig. 11b), pentagon–heptagon defects[125] and pentagon–octagon–pentagon defects.[125] Note that those defects can be aligned and extended to constitute topological line defects and grain boundaries.[126] Line defects in 2D materials include edge dislocations (Fig. 11d), and screw dislocations (material thickness ≥ bilayer, Fig. 11e and f) that have been observed as a domain wall for phase transition,[127] or as a nucleation site for 'spiral' 2D materials growth.[128,129]

There are two pathways to enhance the strength of the materials: one is to design the arrangement of defects to inhibit dislocation motion or cancel defect effects;[130] the other is to go from the opposite: eliminating the defect in crystals using high-quality single-crystal 2D materials. Since it is challenging to prepare large-size single crystal 2D materials for device applications, a usage of polycrystalline 2D crystals is often necessary,[131–133] and therefore understanding the role of defects and GBs in mechanical performance is important. There have been theoretical works demonstrating that the detailed arrangement of defects, *e.g.* the pentagon–heptagon defects associated with graphene GBs, can increase the strength (Fig. 11h),[131–133] although it is highly challenging to achieve such a precise defect engineering in materials for real applications.

In contrast to much research interest in theoretical works, the related experimental works on the effects of defect and

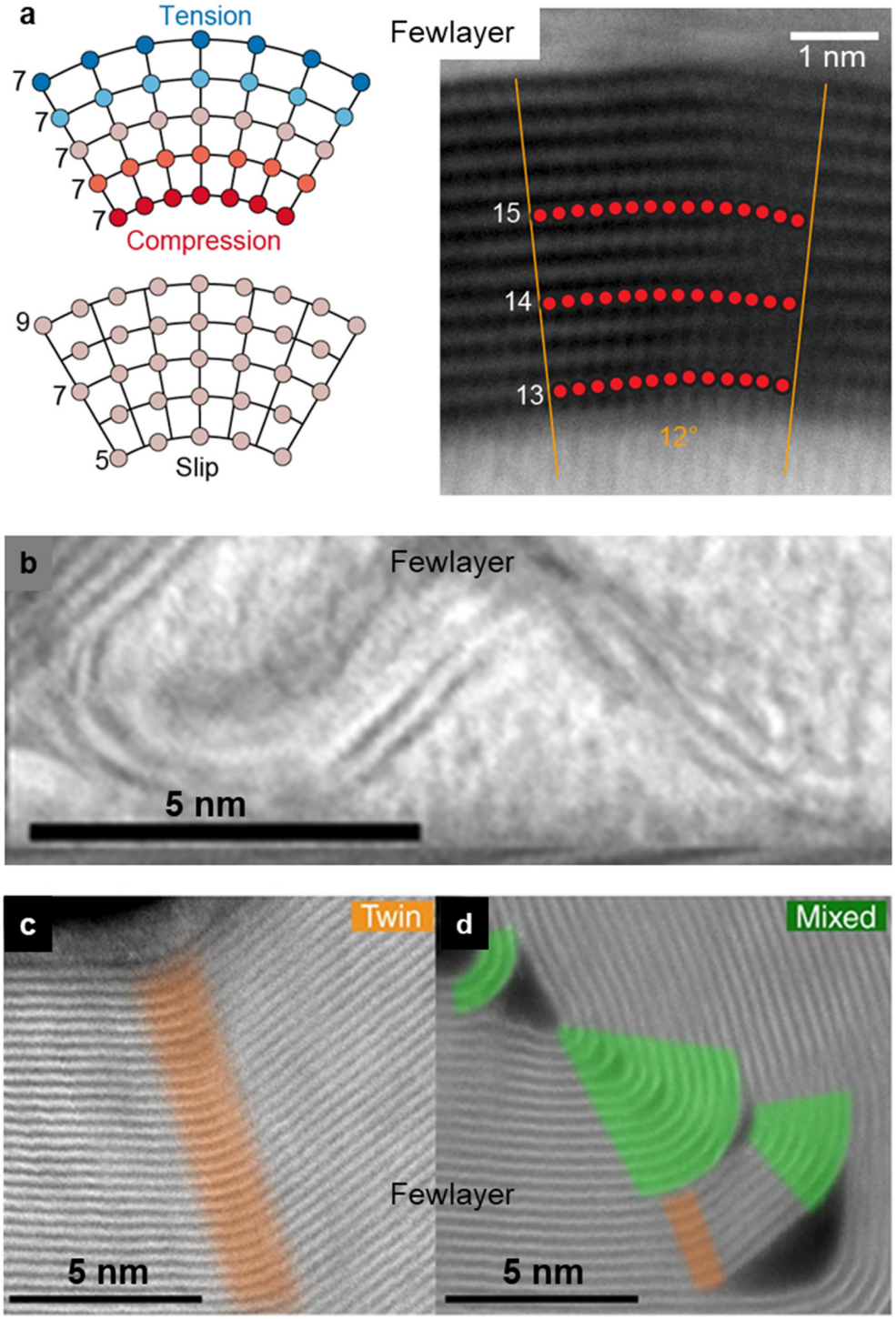

Fig. 10 Deformation mechanisms under bending. (a) Bending in graphene that is subjected to various interlayer interactions. The left top panel shows a model where bending is accommodated by in-plane strain. The left bottom panel shows a model where bending is accommodated through interlayer shear and slip. Experimental STEM image taken from a 12-layer graphene bent to 12° (right panel).[87] (b–d) Cross-sectional STEM images demonstrating the different ways for 2D materials to accommodate the strain induced by bending. Scale bars, 5 nm. (b) BF STEM image taken from bilayer graphene, with a 95° bend angle. (c) HAADF STEM image showing the formation of a twin structure in multilayer graphite subjected to bending. (d) HAADF STEM image taken from multilayer graphite subjected to a large bending deformation, constituting areas of discrete twin boundaries (orange) and areas of nanotube-like curvature (green).[121]

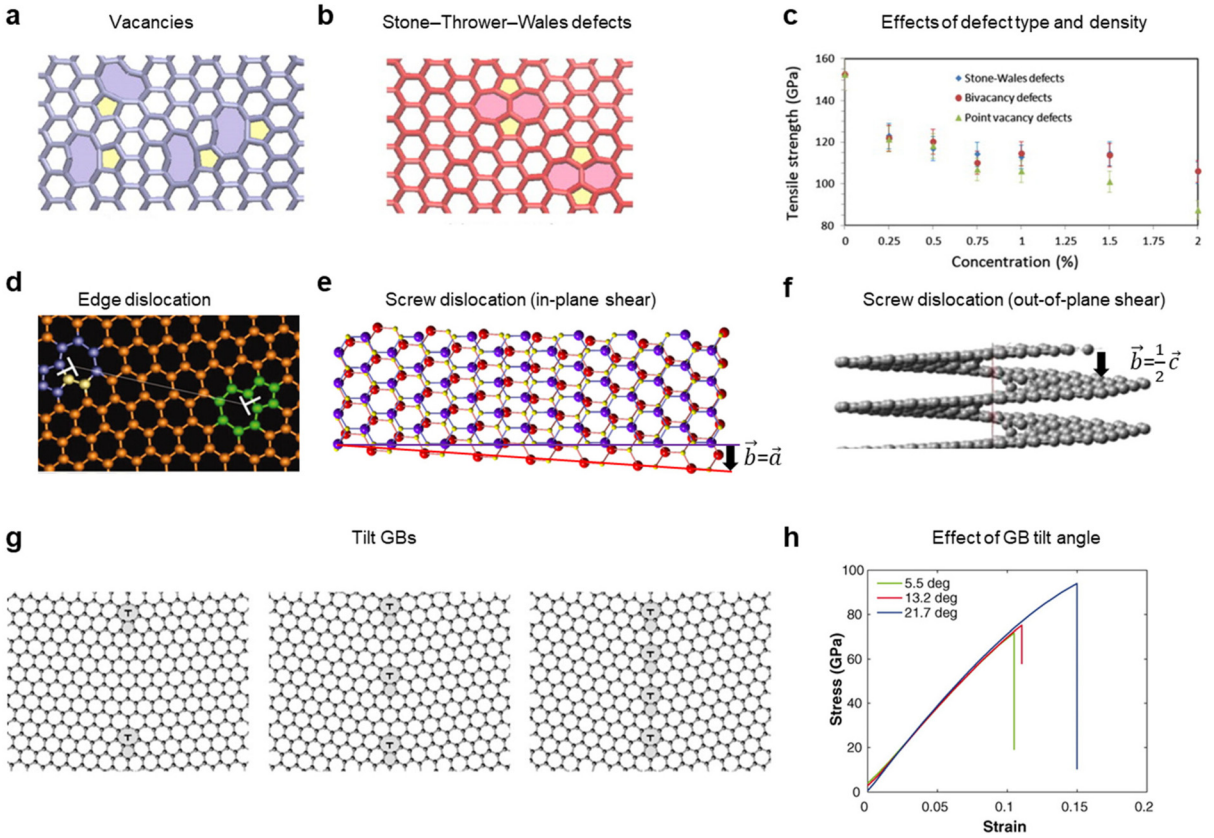

Fig. 11 Theoretical understanding of a defect's impact on mechanical performance. (a) Schematic atomic model of the vacancies in graphene.[123] (b) Schematic atomic model of Stone–Thrower–Wales defects in graphene.[123] (c) Tensile strength of graphene at failure, as a function of point vacancy, bivacancy and Stone–Wales defects concentrations in graphene, calculated by MD. Reproduced from ref. 123 with permissions from Elsevier Ltd. Copyright 2013.[123] (d) Atomic model showing a pair of edge dislocations observed in graphene by TEM. Reproduced from ref. 135 with permissions from The American Association for the Advancement of Science Copyright 2012.[135] (e) Atomic model of screw dislocations with a Burgers vector parallel to a zigzag direction, acting as a 2H|2H domain wall in twisted bilayer TMDs, observed by STEM.[127] (f) Atomic model of screw dislocation with a Burgers vector parallel to the out-of-plane direction,[136] likely to exist in faulty and disordered graphite. Reproduced from ref. 136 with permissions from American Chemical Society Copyright Copyright 2016.[136–138] (g) Atomic models of zigzag-oriented grain boundaries (GBs) in graphene with a tilt angle of 5.5° (left panel), 13.2° (middle panel), and 21.7° (right panel).[131] (h) Corresponding MD calculated stress–strain curves of zigzag-oriented graphene sheets pulled perpendicular to the GBs. Reproduced from ref. 131 with permissions from The American Association for the Advancement of Science Copyright 2010.[131]

grain boundaries are of limited quantity. Previous experiments show that presence of GBs provides weak points for oxygen attack[111] and impurity segregation, leading to a reduced strength of 2D materials,[111] even though careful sample preparation may achieve materials with a strength close to the pristine ones.[92] From the perspective of defect types, there are *in situ* characterization results showing the insensitivity of 2D materials' stretchability to specific types of defect, as demonstrated in previous sections.[53] Regarding the effect of defect density, counter-intuitively, results reported by López-Polín *et al.* showed that the 2D Young's modulus of graphene increases with an increased density of vacancies created by ion implantation, up to almost twice the initial value when the vacancy content reaches ~0.2%, as shown in Fig. 12.[134] Therefore, controversies still exist regarding the impact of defects on the strength of 2D materials, and more detailed and quantitative studies into defect impacts are needed.

4.3 Interfaces

Extensive interest has been put into exploring vdW heterostructures and homostructures, which are a unique class of artificial solids that can be stacked like 'Lego', allowing controllable material components, stacking order and relative twist angle between adjacent atomic layers. Significant breakthroughs have been achieved in vdW heterostructures, including the observation of low-temperature superconductivity in twisted bilayer graphene, and localization of excitons in twisted bilayer TMDs.[127] This makes mechanics studies of vdW heterostructures timely and important.

However, fracture mechanics of vdW heterostructures have been quite limited.[45,56,139,140] The E^{2D} of the bilayer heterostructure is lower than the sum of the E^{2D} of each layer but comparable to the corresponding bilayers, when a strong interlayer interaction is achieved (Fig. 13). Nevertheless, the inter-

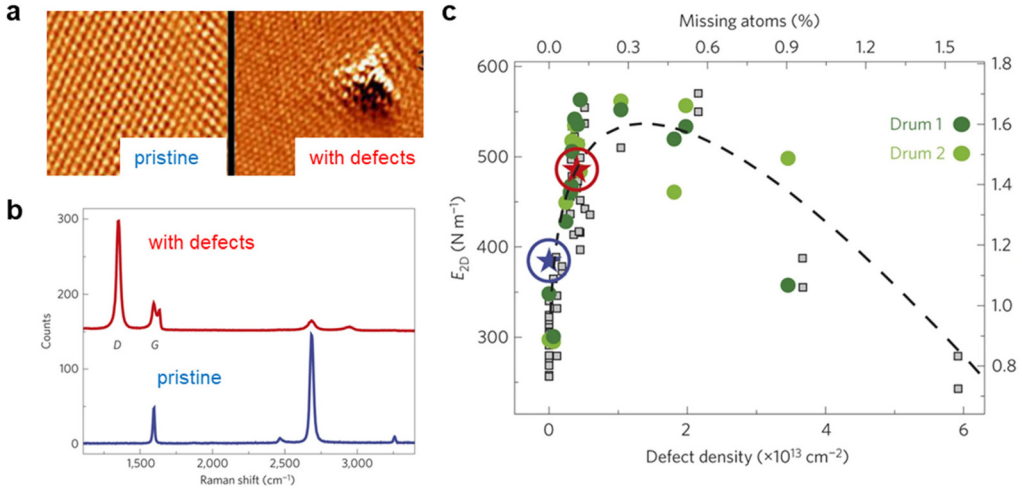

Fig. 12 Experimental understanding of a defect's impact on elastic modulus. (a) Atomic-resolution scanning tunnelling microscopy (STM) characterization of a pristine graphene, before Ar^+ irradiation (left panel), and after irradiation, which shows a single defect containing a vacancy cluster (right panel).[134] (b) Raman spectra taken from the sample before and after the irradiation treatment, denoted by blue and red colours respectively. The intensity ratio between the D and G peaks can be used to evaluate to defect density.[134] (c) E^{2D} measured by AFM nanoindentation as a function of defect concentration. Reproduced from ref. 134 with permissions from Springer Nature Limited Copyright 2014.[134]

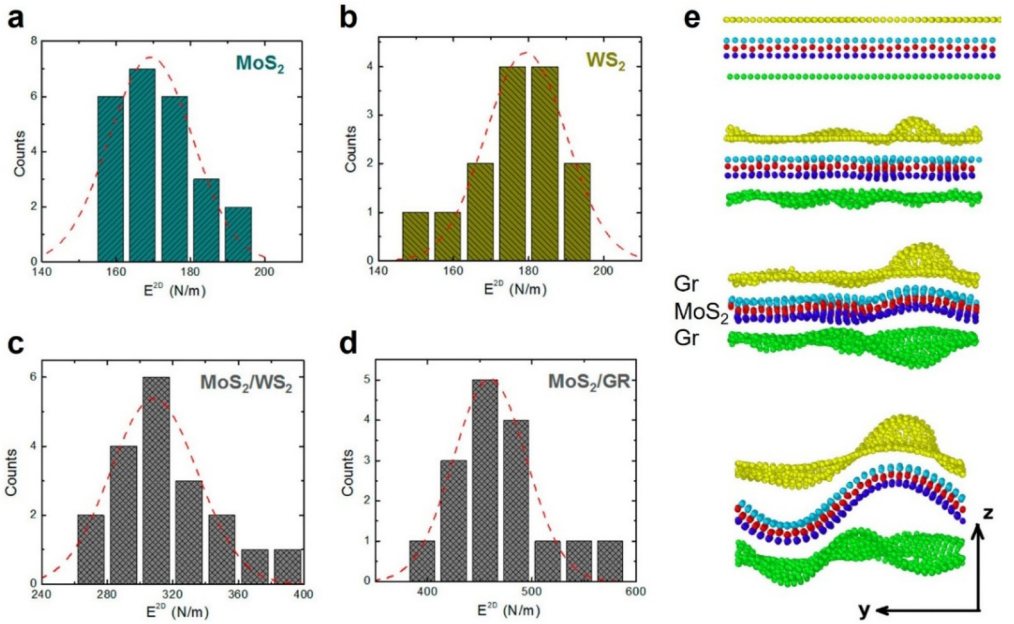

Fig. 13 Elastic properties and fracture failure mechanism in vdW heterostructures. (a–d) Experimentally measured elastic properties for CVD-grown MoS_2 and WS_2 monolayers, and their stacked bilayer heterostructure. (a) Histogram of E^{2D} for CVD MoS_2 nanoplates. (b) Histogram of E^{2D} for CVD WS_2 triangular nanoplates. (c) Histogram of E^{2D} for a CVD MoS_2/WS_2 heterostructure. (d) Histogram of E^{2D} for a CVD MoS_2/Gr heterostructure. Reproduced from ref. 56 with permissions from American Chemical Society Copyright 2014.[56] (e) MD calculated tensile deformation process for a graphene–MoS_2–graphene heterostructure, which shows buckling at the ultimate strain ε = 0.26 at 1.0 K. From top to bottom, the tension in the x direction increases. Reproduced from ref. 139 with permissions from AIP Publishing Copyright 2014.[139]

layer interaction varies with the material components (*e.g.* MoS_2–WS_2 interaction > MoS_2-graphene), and can only be as strong as a homo-bilayer when the interface is clean or coherent (lattice matching). The MD calculation reported showed that local delamination/buckling can happen when the heterostructure is loaded with a large tensile strain (Fig. 13e).

In fact, the interlayer interaction between the stacked components varies with the stacking method and the twist angle.[56] In a twisted heterostructure, for a twist angle close to 0° (identical to $n \times 60°$ with n being an integer, in hexagonal-symmetry 2D materials), lattice matching induces commensurate lattices at the interface, where the interlayer interaction is stronger[141]

compared with the incommensurate interface formed at twist angles deviating from $n \times 60°$. Friction experiments prove that superlubricity exists at graphene–*h*BN heterostructure interfaces for specific twist angles (*e.g.* 30°, 90°, 150°) where the interface is incommensurate (Fig. 14). This used the other mechanical loading mode of AFM, which is nanofriction with the tip moving parallel to the material surface, and meanwhile the horizontal change caused by the frictional force is recorded by the piezoelectric ceramic transducer, suitable for studying the interface characteristics of 2D materials. In contrast, for those twist angles retaining high symmetry (0°, 60°, 120° *etc.*), the interface structure can be commensurate and the friction is found to be much higher (Fig. 14).[142]

Taking advantage of the superlubricity between heterostructures, Huang *et al.* investigated how the bending stiffness of 2D heterostructures evolves with the composition of the stack,[33] following the bending stiffness measurement work shown in section 2. They fabricated four-layer graphene/MoS_2 heterostructures with varied component sequences, including Gr/MoS_2/Gr/MoS_2 (denoted as GMGM here) and Gr/Gr/MoS_2/MoS_2 (GGMM) heterostructures (Fig. 15). MGGM, GMMG, and MMGG show a strong bending angle dependence in bending

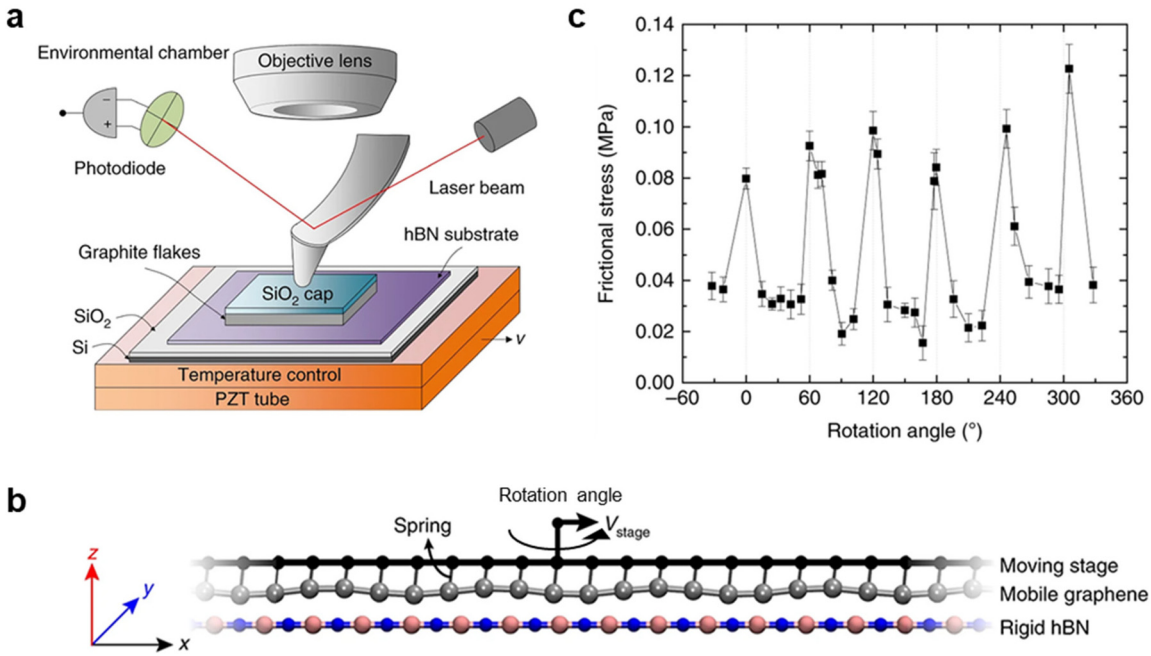

Fig. 14 Measuring the friction at the interface of a graphite/*h*BN heterostructure. (a) Schematic diagram of the experimental set-up to measure the friction in graphite/*h*BN junctions.[142] (b) Schematic atomic model shows the stress loading onto the graphite/*h*BN heterostructures during the friction experiments.[142] (c) Dependence of the frictional stress on the relative interfacial orientation between monocrystalline graphite and *h*BN measured under ambient conditions. Reproduced from ref. 142 with permissions from Springer Nature Limited Copyright 2018.[142]

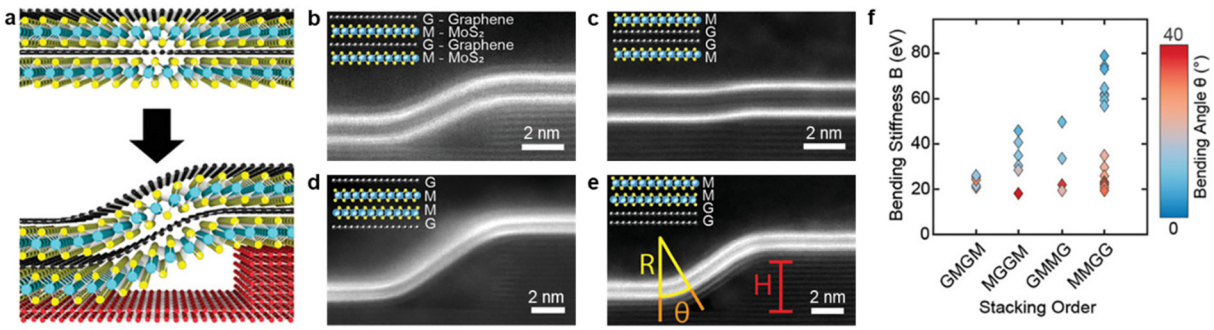

Fig. 15 Bending of four-layer 2D heterostructures, composed of various orders of graphene (G) and MoS_2 (M) layers. (a) Schematic of a heterostructure draped over an atomically sharp step of *h*BN.[33] (b–e) Cross-sectional ADF-STEM images of four different 2D heterostructures (GMGM, MGGM, GMMG, and MMGG) with an identical composition but different stacking orders. Scale bars: 2 nm.[33] (f) Plot of bending stiffness for each heterostructure, coloured by bending angle. Reproduced from ref. 33 with permissions from Wiley-VCH GmbH Copyright 2021.[33]

stiffness. In contrast, the bending stiffness of GMGM exhibits no dependence on the bending angle. At high bending angles, the bending stiffnesses of all four structures converge to approximately 20–25 eV. At low bending angles, the measured bending stiffness is much higher for structures with more aligned interfaces, *i.e.* those containing MM or GG (Fig. 15d). The interfacial friction can be further reduced by large-angle twisting, and the bending stiffness of the resulted heterostructures is largely lower by over several hundred percent compared with other heterostructures. This demonstrates the importance of interfacial engineering in achieving a flexible 2D multilayer, where a minimum bending stiffness can be achieved through misaligning heterointerfaces.

5 Applications

The properties of 2D materials can be changed by strain engineering. To prepare deformed 2D materials, a wide range of approaches has been reported. Besides the direct strain

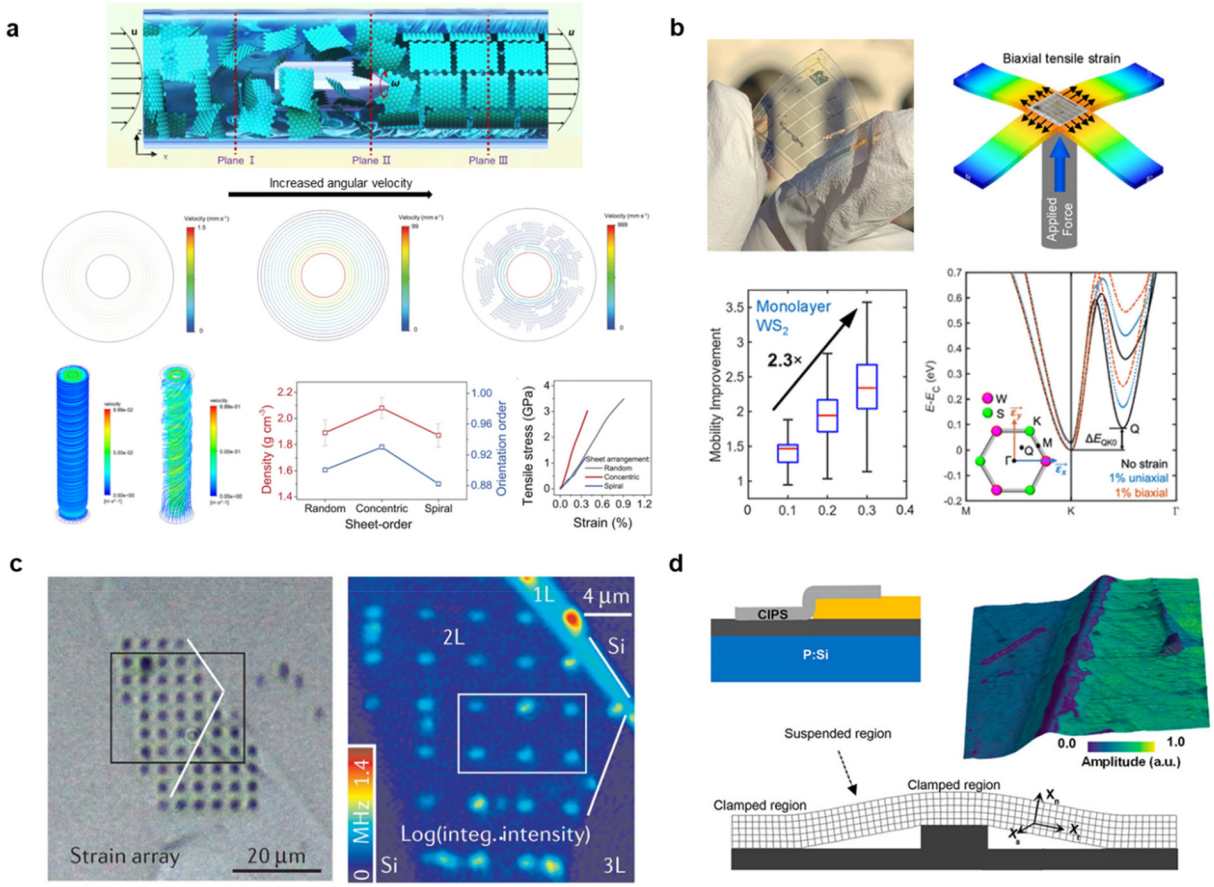

Fig. 16 (a) Rationally constructed high-strength and thermally conductive graphene oxide fibre. The top panel is a schematic showing the sheet-order in the spinning tube under the unidirectional flow field (denoted as Plane I) and the aligned graphene oxide sheets under the multiple flow fields (Planes II and III). The middle panel displays the cross-sectional views of the velocity distributions, calculated under unidirectional tubular shear-flow field (left), and under multiple shear flow with moderate (middle) and overhigh (right) rotating angular velocities. The bottom left panel displays the velocity distribution across the spinning tube calculated under multiple shear-flow with a rotating angular velocity of 100 rad s^{-1} (left) and 1000 rad s^{-1} (right). The bottom middle panel shows the experimentally measured density and orientation order of the graphene fibres. The bottom right panel shows the stress–strain curve measured from the graphene fibres.[38] (b) The top left panel is a digital photo taken from the flexible substrate integrated with hundreds of WS_2 devices. The top right panel is a schematic showing the strain distribution within the WS_2 device under a biaxial strain. The bottom left panel shows the increased mobility as a function of the strain applied to WS_2. Bottom right is a DFT calculation of conduction bands from monolayer WS_2 structures built without strain (black line), with 1% uniaxial strain (dashed blue line), and 1% biaxial strain (dashed orange line) relative to the lowest band edge. The inset is a schematic of the unit cell structure used for the simulation with applied strain vectors. Reproduced from ref. 167 with permissions from American Chemical Society Copyright 2024.[167] (c) Quantum photon emitters fabricated from strain-engineered monolayer and bilayer WSe_2. The left panel is an optical image taken after transfer onto the nanopillars. The right panel is a spatial mapping showing the intensity integrated from the as-measured photoluminescence spectrum between 700–860 nm. Reproduced from ref. 157 with permissions from Springer Nature Limited Copyright 2022.[157,179] (d) Ferroelectricity due to strain in $CuInP_2S_6$. The top left panel shows a schematic of the device structure. The top right panel presents an amplitude map showing the domain wall structure imaged by band excitation piezo-response force microscopy. The bottom panel displays a schematic for the bent nanoflake on the patterned substrate. Reproduced from ref. 172 with permissions from American Chemical Society Copyright 2023.[172]

loading methods described in sections 2 and 3, one can induce the in-plane deformation using the lattice mismatch at an interface of a heterostructure,[90] or at the interface with a substrate.[143,144] Artificial stress can also be applied through force transfer from the supporting substrate or polymer matrix.[115] The out-of-plane deformation can be induced by coherent epitaxy growth,[145] using a substrate with patterned 3D features,[146,147] or a stretchable substrate processed with tension.[148,149] Besides, the strain applied to the 2D materials can be utilized to fabricate crystals with unusual atomic stackings. For example, rhombohedral stacked graphite can be accessed through applying additional shear force during exfoliation[150,151] or during CVD growth on a curved substrate.[152] TMDs with a large-area 3R stacking that is normally thermodynamically metastable can be achieved by internal strain relaxation occurring during the twisting of 2D heterostructures.[127]

To achieve 2D material composites with enhanced flexibility, recent developments on aligning strategy have enabled the rational design of the spatial alignment of 2D materials. Taking graphene fibre as an instance, previous reports have proved the importance of the alignment of graphene sheets to enhance the mechanical properties. This has been achieved through modifying liquid processing parameters, such as shear flow and enlarged crystal concentration in liquid crystal precursors.[153] However, the assembly of sheets remains loose in the transverse direction of the fibre. To improve the order in transverse directions, Gao *et al.* realized the concentric arrangement of graphene oxide nanosheets instead of a random structure through applying a multiple shear flow field.

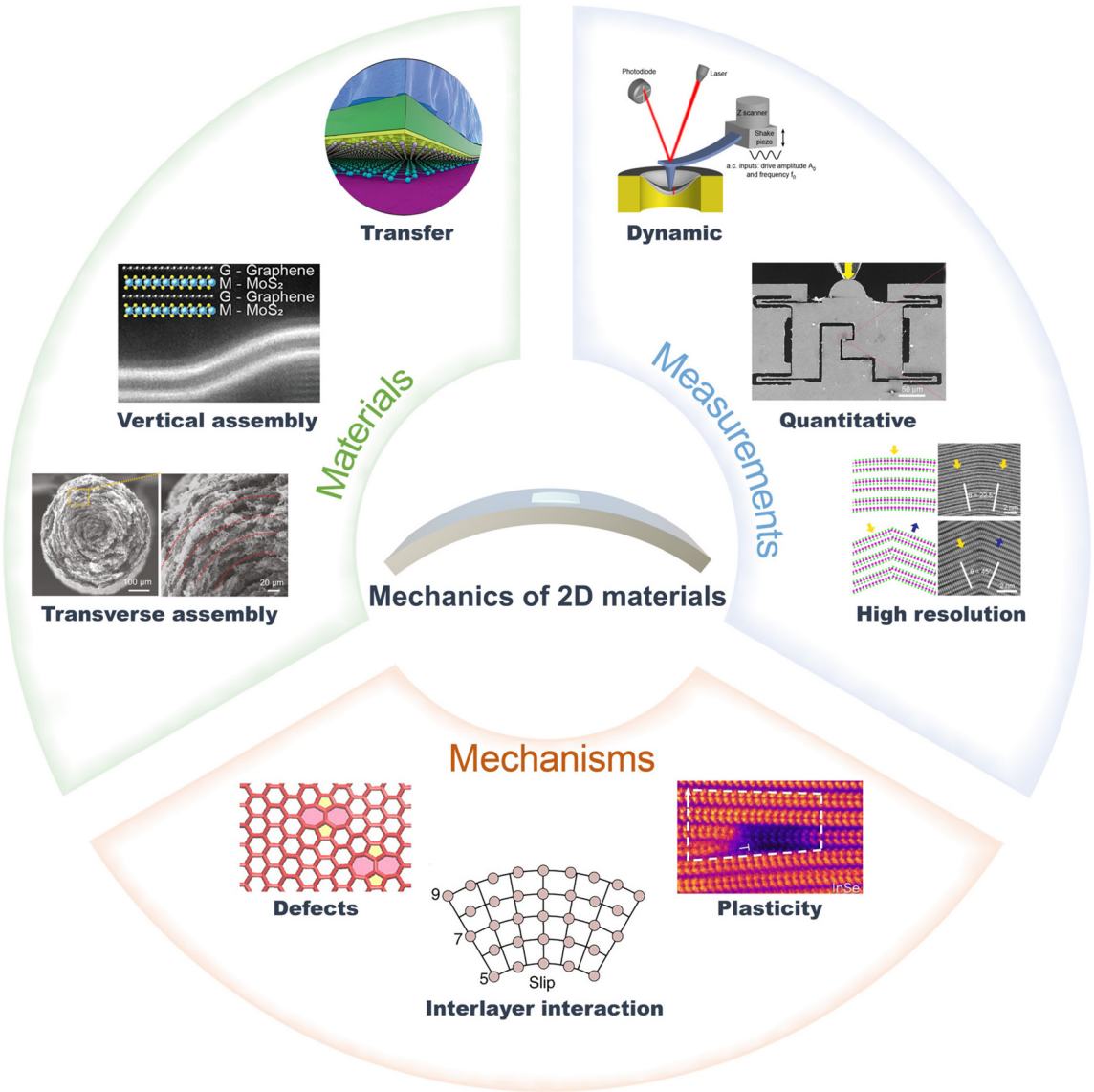

Fig. 17 Strategies and prospects for characterization studies of mechanics in 2D materials. Reproduced from ref. 118 with permissions from American Chemical Society Copyright 2023.[30,32,33,38,51,87,104,118,123]

An increased assembly order is achieved through introducing a rotating angular velocity imposed by rotational shear flow (Fig. 16a).[38] Please note that such an angular velocity–assembly order relationship is non-monotonic. Theoretical modelling indicates that when the angular velocity is too high, the excessive centrifugal force makes the radial pressure gradient and viscous force unable to suppress the disturbance in the flow, resulting in a secondary vortex velocity field and a spiral arrangement with defects.[38] Indeed, experiments show that a higher or lower angular velocity results in the formation of helical disorder or random disorder, which can be characterized by the Hermans orientation function, accounting for the lower thermal conductivity and Young's modulus.[38] Through optimizing the angular velocity, combined with tuning of polymer components in the composites, they achieved an enhanced assembly order in both the longitudinal and transverse directions, and thus synergistically improved and extraordinary mechanical and thermal properties.[38] The above study indicates that it is necessary to correlate the theoretical mechanics with the assembly techniques of 2D flakes for rationally designed structural 2D materials with enhanced mechanical and functional properties.

Deformation has been demonstrated as an established approach to tune the electronic and optical properties of 2D materials, including mobility, photon emitting and ferroelectricity.[154–156] Quite a few theories and experiments have found that strain engineering can be utilized to increase the electron mobility of 2D semiconductors, which allows their applications in flexible electronics and sensors.[157–166] Recently, Yang *et al.* developed a force loading approach that enables a biaxial tensile strain in 2D MoS_2 and WS_2.[167] Compared with the case of uniaxial tensile strain, the mobility of WS_2 can be much higher in biaxial strain status (Fig. 16b).[167] DFT calculations reveal that this resulted from a reduced bandgap as well as a reduced intervalley electron–phonon scattering.[167] For optoelectronic applications, single-photon emitters (SPEs) created by strained 2D materials, including *h*BN, WSe_2, WS_2, and $MoTe_2$, have attracted much interest in the recent decade.[157,159,168–170] This was achieved by suspending 2D semiconductors over arrays of nano-pillars.[159] For example, WSe_2 SPEs were created through transferring a WSe_2 flake on top of lithographically defined nanopillars, where point-like defect or strain perturbations locally change the bandgap and lead to quantum confinement of excitons (Fig. 16c). The performance of the 2D semiconductor SPEs can be modulated by changing the strain applied to the 2D semiconductors. For example, Ferrari *et al.* show that quantum-light emitters with deterministic positions surpass their randomly distributed counterparts, in which case the spectral wanderings were reduced by an order of magnitude.[158] Recently, Chen *et al.* reported that a large local strain of up to 5% in WSe_2 can increase the brightness of the resulting SPEs.[168] They further improved the emitting stability through tightly attaching the 2D semiconductor to the surface of the pillar with enhanced fitting.[168] On the other hand, curvature and strain effects are also important for ferroelectric 2D materials, such as In_2Se_3, $CuInP_2S_6$, and Bi_2TeO_5, and various twisted hetero/homostructures.[100,118,171–177] Enhanced polarization is expected under a large curvature.[171,175] Taking $CuInP_2S_6$ as an example, it was observed that ferroelectric domain boundaries tend to form near or move towards the high-curvature areas, and the polarization–voltage hysteresis loops in the bending regions differ from the non-bending regions (Fig. 16d).[172] The above studies all indicate that achieving precise strain modulation in 2D materials is a crucial strategy for enhancing their performance in electronic and optical devices.[157,167,172,178]

6 Conclusions

In spite of the above progress, studies in the characterization of bendable 2D materials are still in their infancy, with many opportunities and challenges ahead, as summarized in Fig. 17. From the materials' perspective, the limited success in the high-quality transfer of 2D materials onto target substrates, especially onto their characterization platforms like MEMS chips, hinders the investigation into the mechanics of a wider range of 2D materials. The development of handling of 2D materials for experimental mechanics study needs combination with the polymer-free and site-specific transfer methods recently developed for 2D electronics, so that the experiments can reflect the intrinsic properties of the thin materials. Nevertheless, benefiting from the new techniques for the assembly of 2D materials, either vertically or axially, accessibility to materials and devices with high flexibility and enhanced device performances is enlarged nowadays. This allowed the design of the bending stiffness of 2D heterostructures or composites based on a controllable stacking order. Developments in theoretical mechanics are also important for achieving the rational assembly of 2D composites and thus devices with new functionalities. Microscopic studies on characterization methods for mechanics in 2D materials, especially on their response to dynamic stress loading, are necessary in order to understand the mechanical stability of 2D materials for application in resonators and acoustic devices. This further opens the prospects for the development of instruments for quantitative stress loading. Furthermore, correlated imaging is highly needed so that the advantages of various microscopy techniques, such as electron microscopy and optical imaging, can be combined to achieve *in situ* studies with both high spatial and temporal resolutions. It should be noted that the *in situ* imaging protocols specific for 2D materials are not well-established, compared with those for one-dimensional or three-dimensional materials. Mechanisms behind the deformation of 2D materials are not studied systematically considering the controversies and complex effects from defects and interlayer interactions, and have only been investigated for limited types of 2D material. Finally, since those 2D materials with plasticity have their irreplaceability in flexible electronics, the route of integrating them into devices with maintained flexibility and the mechanisms behind the plastic deformation still need exploration.

Data availability

No primary research results, software or code have been included and no new data were generated or analysed as part of this review.

Conflicts of interest

There are no conflicts of interest to declare.

Acknowledgements

This work is supported by the National Natural Science Foundation of China (Grant No. 12474026, 12104517), the Natural Science Foundation of Guangdong Province (Basic and Applied Basic Research Foundation 2023A1515011465) and the Young Top Talents Program 2021QN02C068.

References

1 K. S. Novoselov, A. K. Geim, S. V. Morozov, D. Jiang, Y. Zhang, S. V. Dubonos, I. V. Grigorieva and A. A. Firsov, *Science*, 2004, **306**, 666–669.
2 N. Mounet, M. Gibertini, P. Schwaller, D. Campi, A. Merkys, A. Marrazzo, T. Sohier, I. E. Castelli, A. Cepellotti, G. Pizzi and N. Marzari, *Nat. Nanotechnol.*, 2018, **13**, 246–252.
3 S. B. Desai, S. R. Madhvapathy, A. B. Sachid, J. P. Llinas, Q. Wang, G. H. Ahn, G. Pitner, M. J. Kim, J. Bokor, C. Hu, H.-S. P. Wong and A. Javey, *Science*, 2016, **354**, 99–102.
4 B. Radisavljevic, A. Radenovic, J. Brivio, V. Giacometti and A. Kis, *Nat. Nanotechnol.*, 2011, **6**, 147–150.
5 J. Zhang, N. Kong, S. Uzun, A. Levitt, S. Seyedin, P. A. Lynch, S. Qin, M. Han, W. Yang, J. Liu, X. Wang, Y. Gogotsi and J. M. Razal, *Adv. Mater.*, 2020, **32**, 2001093.
6 C. R. Dean, A. F. Young, I. Meric, C. Lee, L. Wang, S. Sorgenfrei, K. Watanabe, T. Taniguchi, P. Kim, K. L. Shepard and J. Hone, *Nat. Nanotechnol.*, 2010, **5**, 722–726.
7 L. Britnell, R. M. Ribeiro, A. Eckmann, R. Jalil, B. D. Belle, A. Mishchenko, Y.-J. Kim, R. V. Gorbachev, T. Georgiou, S. V. Morozov, A. N. Grigorenko, A. K. Geim, C. Casiraghi, A. H. C. Neto and K. S. Novoselov, *Science*, 2013, **340**, 1311–1314.
8 F. Withers, O. Del Pozo-Zamudio, A. Mishchenko, A. P. Rooney, A. Gholinia, K. Watanabe, T. Taniguchi, S. J. Haigh, A. K. Geim, A. I. Tartakovskii and K. S. Novoselov, *Nat. Mater.*, 2015, **14**, 301–306.
9 N. Lindahl, D. Midtvedt, J. Svensson, O. A. Nerushev, N. Lindvall, A. Isacsson and E. E. B. Campbell, *Nano Lett.*, 2012, **12**, 3526–3531.
10 P. Blake, P. D. Brimicombe, R. R. Nair, T. J. Booth, D. Jiang, F. Schedin, L. A. Ponomarenko, S. V. Morozov, H. F. Gleeson, E. W. Hill, A. K. Geim and K. S. Novoselov, *Nano Lett.*, 2008, **8**, 1704–1708.
11 R. R. Nair, P. Blake, A. N. Grigorenko, K. S. Novoselov, T. J. Booth, T. Stauber, N. M. R. Peres and A. K. Geim, *Science*, 2008, **320**, 1308–1308.
12 P. Z. Sun, Q. Yang, W. J. Kuang, Y. V. Stebunov, W. Q. Xiong, J. Yu, R. R. Nair, M. I. Katsnelson, S. J. Yuan, I. V. Grigorieva, M. Lozada-Hidalgo, F. C. Wang and A. K. Geim, *Nature*, 2020, **579**, 229–232.
13 M. F. El-Kady, V. Strong, S. Dubin and R. B. Kaner, *Science*, 2012, **335**, 1326–1330.
14 K. S. Kim, Y. Zhao, H. Jang, S. Y. Lee, J. M. Kim, K. S. Kim, J.-H. Ahn, P. Kim, J.-Y. Choi and B. H. Hong, *Nature*, 2009, **457**, 706–710.
15 J. N. Coleman, M. Lotya, A. O'Neill, S. D. Bergin, P. J. King, U. Khan, K. Young, A. Gaucher, S. De, R. J. Smith, I. V. Shvets, S. K. Arora, G. Stanton, H.-Y. Kim, K. Lee, G. T. Kim, G. S. Duesberg, T. Hallam, J. J. Boland, J. J. Wang, J. F. Donegan, J. C. Grunlan, G. Moriarty, A. Shmeliov, R. J. Nicholls, J. M. Perkins, E. M. Grieveson, K. Theuwissen, D. W. McComb, P. D. Nellist and V. Nicolosi, *Science*, 2011, **331**, 568–571.
16 Y. Hernandez, V. Nicolosi, M. Lotya, F. M. Blighe, Z. Sun, S. De, I. T. McGovern, B. Holland, M. Byrne, Y. K. Gun'Ko, J. J. Boland, P. Niraj, G. Duesberg, S. Krishnamurthy, R. Goodhue, J. Hutchison, V. Scardaci, A. C. Ferrari and J. N. Coleman, *Nat. Nanotechnol.*, 2008, **3**, 563–568.
17 S. Bae, H. Kim, Y. Lee, X. Xu, J.-S. Park, Y. Zheng, J. Balakrishnan, T. Lei, H. Ri Kim, Y. I. Song, Y.-J. Kim, K. S. Kim, B. Özyilmaz, J.-H. Ahn, B. H. Hong and S. Iijima, *Nat. Nanotechnol.*, 2010, **5**, 574–578.
18 D. Akinwande, N. Petrone and J. Hone, *Nat. Commun.*, 2014, **5**, 5678.
19 J. Yao and G. Yang, *Small*, 2018, **14**, 1704524.
20 F. Liu, W. T. Navaraj, N. Yogeswaran, D. H. Gregory and R. Dahiya, *ACS Nano*, 2019, **13**, 3257–3268.
21 U. Khan, T.-H. Kim, H. Ryu, W. Seung and S.-W. Kim, *Adv. Mater.*, 2017, **29**, 1603544.
22 E. O. Polat, G. Mercier, I. Nikitskiy, E. Puma, T. Galan, S. Gupta, M. Montagut, J. J. Piqueras, M. Bouwens, T. Durduran, G. Konstantatos, S. Goossens and F. Koppens, *Sci. Adv.*, 2019, **5**, eaaw7846.
23 S. K. Ameri, R. Ho, H. Jang, L. Tao, Y. Wang, L. Wang, D. M. Schnyer, D. Akinwande and N. Lu, *ACS Nano*, 2017, **11**, 7634–7641.
24 G. Anagnostopoulos, P.-N. Pappas, Z. Li, I. A. Kinloch, R. J. Young, K. S. Novoselov, C. Y. Lu, N. Pugno, J. Parthenios, C. Galiotis and K. Papagelis, *ACS Appl. Mater. Interfaces*, 2016, **8**, 22605–22614.
25 J. Ryu, Y. Kim, D. Won, N. Kim, J. S. Park, E.-K. Lee, D. Cho, S.-P. Cho, S. J. Kim, G. H. Ryu, H.-A. S. Shin, Z. Lee, B. H. Hong and S. Cho, *ACS Nano*, 2014, **8**, 950–956.
26 T.-R. Wei, M. Jin, Y. Wang, H. Chen, Z. Gao, K. Zhao, P. Qiu, Z. Shan, J. Jiang, R. Li, L. Chen, J. He and X. Shi, *Science*, 2020, **369**, 542–545.

27 A. K. Katiyar, A. T. Hoang, D. Xu, J. Hong, B. J. Kim, S. Ji and J.-H. Ahn, *Chem. Rev.*, 2024, **124**, 318–419.
28 B. Li, J. Li, W. Jiang, Y. Wang, D. Wang, L. Song, Y. Zhu, H. Wu, G. Wang and Z. Zhang, *Nano Lett.*, 2024, **24**, 6344–6352.
29 Y. Yang, B. Liang, J. Kreie, M. Hambsch, Z. Liang, C. Wang, S. Huang, X. Dong, L. Gong, C. Liang, D. Lou, Z. Zhou, J. Lu, Y. Yang, X. Zhuang, H. Qi, U. Kaiser, S. C. B. Mannsfeld, W. Liu, A. Gölzhäuser and Z. Zheng, *Nature*, 2024, **630**, 878–883.
30 L. W. Wong, K. Yang, W. Han, X. Zheng, H. Y. Wong, C. S. Tsang, C.-S. Lee, S. P. Lau, T. H. Ly, M. Yang and J. Zhao, *Nat. Mater.*, 2024, **23**, 196–204.
31 Y. Hou, J. Zhou, Z. He, J. Chen, M. Zhu, H. Wu and Y. Lu, *Nat. Commun.*, 2024, **15**, 4033.
32 T. Cui, S. Mukherjee, P. M. Sudeep, G. Colas, F. Najafi, J. Tam, P. M. Ajayan, C. V. Singh, Y. Sun and T. Filleter, *Nat. Mater.*, 2020, **19**, 405–411.
33 J. Yu, E. Han, M. A. Hossain, K. Watanabe, T. Taniguchi, E. Ertekin, A. M. van der Zande and P. Y. Huang, *Adv. Mater.*, 2021, **33**, 2007269.
34 C. Rong, T. Su, Z. Li, T. Chu, M. Zhu, Y. Yan, B. Zhang and F.-Z. Xuan, *Nat. Commun.*, 2024, **15**, 1566.
35 H. Tang, Y. Wang, X. Ni, K. Watanabe, T. Taniguchi, P. Jarillo-Herrero, S. Fan, E. Mazur, A. Yacoby and Y. Cao, *Nature*, 2024, **632**, 1038–1044.
36 A. J. Mannix, A. Ye, S. H. Sung, A. Ray, F. Mujid, C. Park, M. Lee, J.-H. Kang, R. Shreiner, A. A. High, D. A. Muller, R. Hovden and J. Park, *Nat. Nanotechnol.*, 2022, **17**, 361–366.
37 M. Nakatani, S. Fukamachi, P. Solís-Fernández, S. Honda, K. Kawahara, Y. Tsuji, Y. Sumiya, M. Kuroki, K. Li, Q. Liu, Y.-C. Lin, A. Uchida, S. Oyama, H. G. Ji, K. Okada, K. Suenaga, Y. Kawano, K. Yoshizawa, A. Yasui and H. Ago, *Nat. Electron.*, 2024, **7**, 119–130.
38 P. Li, Z. Wang, Y. Qi, G. Cai, Y. Zhao, X. Ming, Z. Lin, W. Ma, J. Lin, H. Li, K. Shen, Y. Liu, Z. Xu, Z. Xu and C. Gao, *Nat. Commun.*, 2024, **15**, 409.
39 Z. Gao, T.-R. Wei, T. Deng, P. Qiu, W. Xu, Y. Wang, L. Chen and X. Shi, *Nat. Commun.*, 2022, **13**, 7491.
40 Z. Dai, L. Liu and Z. Zhang, *Adv. Mater.*, 2019, **31**, 1805417.
41 C. Si, Z. Sun and F. Liu, *Nanoscale*, 2016, **8**, 3207–3217.
42 C. Lee, X. Wei, J. W. Kysar and J. Hone, *Science*, 2008, **321**, 385–388.
43 M. Z. Miskin, K. J. Dorsey, B. Bircan, Y. Han, D. A. Muller, P. L. McEuen and I. Cohen, *Proc. Natl. Acad. Sci. U. S. A.*, 2018, **115**, 466–470.
44 Y. Yang, Z. Song, G. Lu, Q. Zhang, B. Zhang, B. Ni, C. Wang, X. Li, L. Gu, X. Xie, H. Gao and J. Lou, *Nature*, 2021, **594**, 57–61.
45 C. Androulidakis, K. Zhang, M. Robertson and S. Tawfick, *2D Mater.*, 2018, **5**, 032005.
46 M. Holwill, *Nanomechanics in van der Waals heterostructures*, Springer, Cham, 2019.
47 A. Castellanos-Gomez, V. Singh, H. S. J. van der Zant and G. A. Steele, *Ann. Phys.*, 2015, **527**, 27–44.
48 J. Tan, H. Zhang, X. Wang, Y. Wang, J.-J. Wang, H. Zhang, E. Ma and W. Zhang, *Mater. Today*, 2024, **80**, 250–261.
49 Y. Sun, J. Pan, Z. Zhang, K. Zhang, J. Liang, W. Wang, Z. Yuan, Y. Hao, B. Wang, J. Wang, Y. Wu, J. Zheng, L. Jiao, S. Zhou, K. Liu, C. Cheng, W. Duan, Y. Xu, Q. Yan and K. Liu, *Nano Lett.*, 2019, **19**, 761–769.
50 A. Falin, Q. Cai, E. J. Santos, D. Scullion, D. Qian, R. Zhang, Z. Yang, S. Huang, K. Watanabe, T. Taniguchi, M. R. Barnett, Y. Chen, R. S. Ruoff and L. H. Li, *Nat. Commun.*, 2017, **8**, 15815.
51 K. Cao, S. Feng, Y. Han, L. Gao, T. H. Ly, Z. Xu and Y. Lu, *Nat. Commun.*, 2020, **11**, 284.
52 G. Wang, Z. Dai, Y. Wang, P. Tan, L. Liu, Z. Xu, Y. Wei, R. Huang and Z. Zhang, *Phys. Rev. Lett.*, 2017, **119**, 036101.
53 Y. Han, S. Feng, K. Cao, Y. Wang, L. Gao, Z. Xu and Y. Lu, *Cell Rep. Phys. Sci.*, 2020, **1**, 100172.
54 G. Wang, Z. Dai, J. Xiao, S. Feng, C. Weng, L. Liu, Z. Xu, R. Huang and Z. Zhang, *Phys. Rev. Lett.*, 2019, **123**, 116101.
55 S. Bertolazzi, J. Brivio and A. Kis, *ACS Nano*, 2011, **5**, 9703–9709.
56 K. Liu, Q. Yan, M. Chen, W. Fan, Y. Sun, J. Suh, D. Fu, S. Lee, J. Zhou, S. Tongay, J. Ji, J. B. Neaton and J. Wu, *Nano Lett.*, 2014, **14**, 5097–5103.
57 D. Lloyd, X. Liu, N. Boddeti, L. Cantley, R. Long, M. L. Dunn and J. S. Bunch, *Nano Lett.*, 2017, **17**, 5329–5334.
58 N. Iguiñiz, R. Frisenda, R. Bratschitsch and A. Castellanos-Gomez, *Adv. Mater.*, 2019, **31**, 1807150.
59 Y. Li, C. Yu, Y. Gan, P. Jiang, J. Yu, Y. Ou, D.-F. Zou, C. Huang, J. Wang, T. Jia, Q. Luo, X.-F. Yu, H. Zhao, C.-F. Gao and J. Li, *npj Comput. Mater.*, 2018, **4**, 49.
60 Y. Yang, X. Li, M. Wen, E. Hacopian, W. Chen, Y. Gong, J. Zhang, B. Li, W. Zhou, P. M. Ajayan, Q. Chen, T. Zhu and J. Lou, *Adv. Mater.*, 2017, **29**, 1604201.
61 V. Babacic, D. S. Reig, S. Varghese, T. Vasileiadis, E. Coy, K.-J. Tielrooij and B. Graczykowski, *Adv. Mater.*, 2021, **33**, 2008614.
62 J. Li, N. V. Medhekar and V. B. Shenoy, *J. Phys. Chem. C*, 2013, **117**, 15842–15848.
63 R. Zhang, V. Koutsos and R. Cheung, *Appl. Phys. Lett.*, 2016, **108**, 042104.
64 A. Falin, M. Holwill, H. Lv, W. Gan, J. Cheng, R. Zhang, D. Qian, M. R. Barnett, E. J. G. Santos, K. S. Novoselov, T. Tao, X. Wu and L. H. Li, *ACS Nano*, 2021, **15**, 2600–2610.
65 H. Wang, E. J. Sandoz-Rosado, S. H. Tsang, J. Lin, M. Zhu, G. Mallick, Z. Liu and E. H. T. Teo, *Adv. Funct. Mater.*, 2019, **29**, 1902663.
66 Y. M. Jahn and A. Ya'Akobovitz, *Nanoscale*, 2021, **13**, 18458–18466.
67 G. Wang, Z. Zhang, Y. Wang, E. Gao, X. Jia, Z. Dai, C. Weng, L. Liu, Y. Zhang and Z. Zhang, *ACS Appl. Mater. Interfaces*, 2021, **13**, 3040–3050.
68 Y. Li, C. Yu, Y. Gan, Y. Kong, P. Jiang, D.-F. Zou, P. Li, X.-F. Yu, R. Wu and H. Zhao, *Nanotechnology*, 2019, **30**, 335703.

69 B. Chitara and A. Ya'Akobovitz, *Nanoscale*, 2018, **10**, 13022–13027.
70 L. Guo, H. Yan, Q. Moore, M. Buettner, J. Song, L. Li, P. T. Araujo and H.-T. Wang, *Nanoscale*, 2015, **7**, 11915–11921.
71 H. Yan, C. Vajner, M. Kuhlman, L. Guo, L. Li, P. T. Araujo and H.-T. Wang, *Appl. Phys. Lett.*, 2016, **109**, 032103.
72 J.-Y. Wang, Y. Li, Z.-Y. Zhan, T. Li, L. Zhen and C.-Y. Xu, *Appl. Phys. Lett.*, 2016, **108**, 013104.
73 B. Zhang, L. Zhang, N. Yang, X. Zhao, C. Chen, Y. Cheng, I. Rasheed, L. Ma and J. Zhang, *J. Phys. Chem. C*, 2022, **126**, 1094–1098.
74 A. Lipatov, H. Lu, M. Alhabeb, B. Anasori, A. Gruverman, Y. Gogotsi and A. Sinitskii, *Sci. Adv.*, 2018, **4**, eaat0491.
75 A. Lipatov, M. Alhabeb, H. Lu, S. Zhao, M. Loes, N. Vorobeva, Y. Dall'Agnese, Y. Gao, A. Gruverman, Y. Gogotsi and A. Sinitskii, *Adv. Electron. Mater.*, 2020, **6**, 1901382.
76 A. Castellanos-Gomez, M. Poot, A. Amor-Amorós, G. A. Steele, H. S. J. van der Zant, N. Agraït and G. Rubio-Bollinger, *Nano Res.*, 2012, **5**, 550–557.
77 Q. Hao, C. Zhao, B. Sun, C. Lu, J. Liu, M. Liu, L.-J. Wan and D. Wang, *J. Am. Chem. Soc.*, 2018, **140**, 12152–12158.
78 Z. Zeng, I. S. Flyagina and J.-C. Tan, *Nanoscale Adv.*, 2020, **2**, 5181–5191.
79 Q. Tu, I. Spanopoulos, P. Yasaei, C. C. Stoumpos, M. G. Kanatzidis, G. S. Shekhawat and V. P. Dravid, *ACS Nano*, 2018, **12**, 10347–10354.
80 W. Chen, U. Khan, S. Feng, B. Ding, X. Xu and B. Liu, *Adv. Funct. Mater.*, 2020, **30**, 2004960.
81 M. Šiškins, S. Kurdi, M. Lee, B. J. M. Slotboom, W. Xing, S. Mañas-Valero, E. Coronado, S. Jia, W. Han, T. van der Sar, H. S. J. van der Zant and P. G. Steeneken, *npj 2D Mater. Appl.*, 2022, **6**, 41.
82 F. Cantos-Prieto, A. Falin, M. Alliati, D. Qian, R. Zhang, T. Tao, M. R. Barnett, E. J. Santos, L. H. Li and E. Navarro-Moratalla, *Nano Lett.*, 2021, **21**, 3379–3385.
83 M. Šiškins, M. Lee, F. Alijani, M. R. van Blankenstein, D. Davidovikj, H. S. J. van der Zant and P. G. Steeneken, *ACS Nano*, 2019, **13**, 10845–10851.
84 T. Hu, J. Yang, W. Li, X. Wang and C. M. Li, *Phys. Chem. Chem. Phys.*, 2020, **22**, 2115–2121.
85 Y. Wei, B. Wang, J. Wu, R. Yang and M. L. Dunn, *Nano Lett.*, 2013, **13**, 26–30.
86 X. Chen, C. Yi and C. Ke, *Appl. Phys. Lett.*, 2015, **106**, 101907.
87 E. Han, J. Yu, E. Annevelink, J. Son, D. A. Kang, K. Watanabe, T. Taniguchi, E. Ertekin, P. Y. Huang and A. M. van der Zande, *Nat. Mater.*, 2020, **19**, 305–309.
88 Y. Huang, Y.-H. Pan, R. Yang, L.-H. Bao, L. Meng, H.-L. Luo, Y.-Q. Cai, G.-D. Liu, W.-J. Zhao, Z. Zhou, L.-M. Wu, Z.-L. Zhu, M. Huang, L.-W. Liu, L. Liu, P. Cheng, K.-H. Wu, S.-B. Tian, C.-Z. Gu, Y.-G. Shi, Y.-F. Guo, Z. G. Cheng, J.-P. Hu, L. Zhao, G.-H. Yang, E. Sutter, P. Sutter, Y.-L. Wang, W. Ji, X.-J. Zhou and H.-J. Gao, *Nat. Commun.*, 2020, **11**, 2453.
89 M. Velický, G. E. Donnelly, W. R. Hendren, S. McFarland, D. Scullion, W. J. I. DeBenedetti, G. C. Correa, Y. Han, A. J. Wain, M. A. Hines, D. A. Muller, K. S. Novoselov, H. D. Abruña, R. M. Bowman, E. J. G. Santos and F. Huang, *ACS Nano*, 2018, **12**, 10463–10472.
90 X. Li, M.-W. Lin, J. Lin, B. Huang, A. A. Puretzky, C. Ma, K. Wang, W. Zhou, S. T. Pantelides, M. Chi, I. Kravchenko, J. Fowlkes, C. M. Rouleau, D. B. Geohegan and K. Xiao, *Sci. Adv.*, 2016, **2**, e1501882.
91 Y. Huang, E. Sutter, N. N. Shi, J. Zheng, T. Yang, D. Englund, H.-J. Gao and P. Sutter, *ACS Nano*, 2015, **9**, 10612–10620.
92 G.-H. Lee, R. C. Cooper, S. J. An, S. Lee, A. van der Zande, N. Petrone, A. G. Hammerberg, C. Lee, B. Crawford, W. Oliver, J. W. Kysar and J. Hone, *Science*, 2013, **340**, 1073–1076.
93 A. Castellanos-Gomez, M. Poot, G. A. Steele, H. S. J. van der Zant, N. Agraït and G. Rubio-Bollinger, *Nanoscale Res. Lett.*, 2012, **7**, 233.
94 P. Zhang, L. Ma, F. Fan, Z. Zeng, C. Peng, P. E. Loya, Z. Liu, Y. Gong, J. Zhang, X. Zhang, P. M. Ajayan, T. Zhu and J. Lou, *Nat. Commun.*, 2014, **5**, 3782.
95 A. Zandiatashbar, G.-H. Lee, S. J. An, S. Lee, N. Mathew, M. Terrones, T. Hayashi, C. R. Picu, J. Hone and N. Koratkar, *Nat. Commun.*, 2014, **5**, 3186.
96 S. P. Koenig, N. G. Boddeti, M. L. Dunn and J. S. Bunch, *Nat. Nanotechnol.*, 2011, **6**, 543–546.
97 Z. Song, V. I. Artyukhov, J. Wu, B. I. Yakobson and Z. Xu, *ACS Nano*, 2015, **9**, 401–408.
98 J. Han, N. M. Pugno and S. Ryu, *Nanoscale*, 2015, **7**, 15672–15679.
99 G. López-Polín, J. Gómez-Herrero and C. Gómez-Navarro, *Nano Lett.*, 2015, **15**, 2050–2054.
100 X. Zheng, W. Han, K. Yang, L. W. Wong, C. S. Tsang, K. H. Lai, F. Zheng, T. Yang, S. P. Lau, T. H. Ly, M. Yang and J. Zhao, *Sci. Adv.*, 2022, **8**, eabo0773.
101 S. R. Sadanand, B. J. Cheol, Y. G. Yeol, R. Jae-Kyung, L. C. Jun, H. Seong-Gu, B. Sachin and K. T. Nam, *Korean J. Mater. Res.*, 2018, **28**, 627–632.
102 Z. Wan, H. Liu, Y. Zheng, Y. Ma, K. Liu, X. Zhou, C. Liu, K. Liu and E. Wang, *Adv. Funct. Mater.*, 2024, **34**, 2303519.
103 T. F. Schranghamer, M. Sharma, R. Singh and S. Das, *Chem. Soc. Rev.*, 2021, **50**, 11032–11054.
104 W. Wang, N. Clark, M. Hamer, A. Carl, E. Tovari, S. Sullivan-Allsop, E. Tillotson, Y. Gao, H. de Latour, F. Selles, J. Howarth, E. G. Castanon, M. Zhou, H. Bai, X. Li, A. Weston, K. Watanabe, T. Taniguchi, C. Mattevi, T. H. Bointon, P. V. Wiper, A. J. Strudwick, L. A. Ponomarenko, A. V. Kretinin, S. J. Haigh, A. Summerfield and R. Gorbachev, *Nat. Electron.*, 2023, **6**, 981–990.
105 M. J. Hamer, D. G. Hopkinson, N. Clark, M. Zhou, W. Wang, Y. Zou, D. J. Kelly, T. H. Bointon, S. J. Haigh and R. V. Gorbachev, *Nano Lett.*, 2020, **20**, 6582–6589.
106 P. Li, C. Jiang, S. Xu, Y. Zhuang, L. Gao, A. Hu, H. Wang and Y. Lu, *Nanoscale*, 2017, **9**, 9119–9128.

107 Q. Fang, C. Sui, C. Wang, T. Zhai, J. Zhang, J. Liang, H. Guo, E. Sandoz-Rosado and J. Lou, *Matter*, 2021, **4**, 1017–1028.
108 D. G. Papageorgiou, I. A. Kinloch and R. J. Young, *Prog. Mater. Sci.*, 2017, **90**, 75–127.
109 K. L. Firestein, J. E. von Treifeldt, D. G. Kvashnin, J. F. S. Fernando, C. Zhang, A. G. Kvashnin, E. V. Podryabinkin, A. V. Shapeev, D. P. Siriwardena, P. B. Sorokin and D. Golberg, *Nano Lett.*, 2020, **20**, 5900–5908.
110 X. Liu, T. H. Metcalf, J. T. Robinson, B. H. Houston and F. Scarpa, *Nano Lett.*, 2012, **12**, 1013–1017.
111 Z. Li, R. J. Young, C. Backes, W. Zhao, X. Zhang, A. Zhukov, E. Tillotson, A. P. Conlan, F. Ding, S. J. Haigh, K. S. Novoselov and J. N. Coleman, *ACS Nano*, 2020, **14**, 10976–10985.
112 K. Min and N. R. Aluru, *Appl. Phys. Lett.*, 2011, **98**, 013113.
113 L. He, S. Guo, J. Lei, Z. Sha and Z. Liu, *Carbon*, 2014, **75**, 124–132.
114 H. Yin, H. J. Qi, F. Fan, T. Zhu, B. Wang and Y. Wei, *Nano Lett.*, 2015, **15**, 1918–1924.
115 L. Gong, R. J. Young, I. A. Kinloch, S. J. Haigh, J. H. Warner, J. A. Hinks, Z. Xu, L. Li, F. Ding, I. Riaz, R. Jalil and K. S. Novoselov, *ACS Nano*, 2013, **7**, 7287–7294.
116 I. V. Lebedeva, A. V. Lebedev, A. M. Popov and A. A. Knizhnik, *Phys. Rev. B*, 2016, **93**, 235414.
117 P. Li, K. Cao, C. Jiang, S. Xu, L. Gao, X. Xiao and Y. Lu, *Nanotechnology*, 2019, **30**, 475708.
118 E. Han, S. M. Nahid, T. Rakib, G. Nolan, P. F. Ferrari, M. A. Hossain, A. Schleife, S. Nam, E. Ertekin, A. M. van der Zande and P. Y. Huang, *ACS Nano*, 2023, **17**, 7881–7888.
119 D.-M. Tang, D. G. Kvashnin, S. Najmaei, Y. Bando, K. Kimoto, P. Koskinen, P. M. Ajayan, B. I. Yakobson, P. B. Sorokin, J. Lou and D. Golberg, *Nat. Commun.*, 2014, **5**, 3631.
120 C. Yi, C. Hu, M. Bai, J. Lv and D. Tang, *Nanotechnology*, 2020, **31**, 215703.
121 A. P. Rooney, Z. Li, W. Zhao, A. Gholinia, A. Kozikov, G. Auton, F. Ding, R. V. Gorbachev, R. J. Young and S. J. Haigh, *Nat. Commun.*, 2018, **9**, 3597.
122 V. Sorkin, Q. X. Pei and Y. W. Zhang, in *Handbook of Materials Modeling: Applications: Current and Emerging Materials*, ed. W. Andreoni and S. Yip, Springer International Publishing, Cham, 2020, pp. 1869–1909.
123 B. Mortazavi and S. Ahzi, *Carbon*, 2013, **63**, 460–470.
124 C. Cao, S. Mukherjee, J. Y. Howe, D. D. Perovic, Y. Sun, C. V. Singh and T. Filleter, *Sci. Adv.*, 2018, **4**, eaao7202.
125 H. Terrones, R. Lv, M. Terrones and M. S. Dresselhaus, *Rep. Prog. Phys.*, 2012, **75**, 062501.
126 J. Lahiri, Y. Lin, P. Bozkurt, I. I. Oleynik and M. Batzill, *Nat. Nanotechnol.*, 2010, **5**, 326–329.
127 A. Weston, Y. Zou, V. Enaldiev, A. Summerfield, N. Clark, V. Zólyomi, A. Graham, C. Yelgel, S. Magorrian, M. Zhou, J. Zultak, D. Hopkinson, A. Barinov, T. H. Bointon, A. Kretinin, N. R. Wilson, P. H. Beton, V. I. Fal'ko, S. J. Haigh and R. Gorbachev, *Nat. Nanotechnol.*, 2020, **15**, 592–597.
128 T. H. Ly, J. Zhao, H. Kim, G. H. Han, H. Nam and Y. H. Lee, *Adv. Mater.*, 2016, **28**, 7723–7728.
129 R. Y. Tay, H. J. Park, J. Lin, Z. K. Ng, L. Jing, H. Li, M. Zhu, S. H. Tsang, Z. Lee and E. H. T. Teo, *Chem. Mater.*, 2018, **30**, 6858–6866.
130 T. Deng, Z. Gao, Z. Li, P. Qiu, Z. Li, X. Yuan, C. Ming, T.-R. Wei, L. Chen and X. Shi, *Science*, 2024, **386**, 1112–1117.
131 R. Grantab, V. B. Shenoy and R. S. Ruoff, *Science*, 2010, **330**, 946–948.
132 Y. Wei, J. Wu, H. Yin, X. Shi, R. Yang and M. Dresselhaus, *Nat. Mater.*, 2012, **11**, 759–763.
133 T.-H. Liu, C.-W. Pao and C.-C. Chang, *Carbon*, 2012, **50**, 3465–3472.
134 G. López-Polín, C. Gómez-Navarro, V. Parente, F. Guinea, M. I. Katsnelson, F. Pérez-Murano and J. Gómez-Herrero, *Nat. Phys.*, 2015, **11**, 26–31.
135 J. H. Warner, E. R. Margine, M. Mukai, A. W. Robertson, F. Giustino and A. I. Kirkland, *Science*, 2012, **337**, 209–212.
136 F. Xu, H. Yu, A. Sadrzadeh and B. I. Yakobson, *Nano Lett.*, 2016, **16**, 34–39.
137 I. Suarez-Martinez, G. Savini, G. Haffenden, J. M. Campanera and M. I. Heggie, *Phys. Status Solidi C*, 2007, **4**, 2958–2962.
138 J. W. Martin, C. de Tomas, I. Suarez-Martinez, M. Kraft and N. A. Marks, *Phys. Rev. Lett.*, 2019, **123**, 116105.
139 J.-W. Jiang and H. S. Park, *Appl. Phys. Lett.*, 2014, **105**, 033108.
140 T. Mukhopadhyay, A. Mahata, S. Adhikari and M. A. Zaeem, *Nanoscale*, 2018, **10**, 5280–5294.
141 J. Zhang, J. Wang, P. Chen, Y. Sun, S. Wu, Z. Jia, X. Lu, H. Yu, W. Chen, J. Zhu, G. Xie, R. Yang, D. Shi, X. Xu, J. Xiang, K. Liu and G. Zhang, *Adv. Mater.*, 2016, **28**, 1950–1956.
142 Y. Song, D. Mandelli, O. Hod, M. Urbakh, M. Ma and Q. Zheng, *Nat. Mater.*, 2018, **17**, 894–899.
143 G. H. Ahn, M. Amani, H. Rasool, D.-H. Lien, J. P. Mastandrea, J. W. Ager III, M. Dubey, D. C. Chrzan, A. M. Minor and A. Javey, *Nat. Commun.*, 2017, **8**, 608.
144 Y. K. Ryu, F. Carrascoso, R. López-Nebreda, N. Agraït, R. Frisenda and A. Castellanos-Gomez, *Nano Lett.*, 2020, **20**, 5339–5345.
145 S. Xie, L. Tu, Y. Han, L. Huang, K. Kang, K. U. Lao, P. Poddar, C. Park, D. A. Muller, R. A. DiStasio and J. Park, *Science*, 2018, **359**, 1131–1136.
146 J. Choi, H. J. Kim, M. C. Wang, J. Leem, W. P. King and S. Nam, *Nano Lett.*, 2015, **15**, 4525–4531.
147 Y. Zhang, M. Heiranian, B. Janicek, Z. Budrikis, S. Zapperi, P. Y. Huang, H. T. Johnson, N. R. Aluru, J. W. Lyding and N. Mason, *Nano Lett.*, 2018, **18**, 2098–2104.
148 A. Castellanos-Gomez, R. Roldán, E. Cappelluti, M. Buscema, F. Guinea, H. S. J. van der Zant and G. A. Steele, *Nano Lett.*, 2013, **13**, 5361–5366.

149 Y. Wang, R. Yang, Z. Shi, L. Zhang, D. Shi, E. Wang and G. Zhang, *ACS Nano*, 2011, **5**, 3645–3650.
150 S. Huang, G. Zhang, F. Fan, C. Song, F. Wang, Q. Xing, C. Wang, H. Wu and H. Yan, *Nat. Commun.*, 2019, **10**, 2447.
151 J. P. Nery, M. Calandra and F. Mauri, *Nano Lett.*, 2020, **20**, 5017–5023.
152 Z. Gao, S. Wang, J. Berry, Q. Zhang, J. Gebhardt, W. M. Parkin, J. Avila, H. Yi, C. Chen, S. Hurtado-Parra, M. Drndić, A. M. Rappe, D. J. Srolovitz, J. M. Kikkawa, Z. Luo, M. C. Asensio, F. Wang and A. T. C. Johnson, *Nat. Commun.*, 2020, **11**, 546.
153 A. Akbari, P. Sheath, S. T. Martin, D. B. Shinde, M. Shaibani, P. C. Banerjee, R. Tkacz, D. Bhattacharyya and M. Majumder, *Nat. Commun.*, 2016, **7**, 10891.
154 Y. Dong, M.-M. Yang, M. Yoshii, S. Matsuoka, S. Kitamura, T. Hasegawa, N. Ogawa, T. Morimoto, T. Ideue and Y. Iwasa, *Nat. Nanotechnol.*, 2023, **18**, 36–41.
155 J. Zhu, S. Wu, L. Wang, J. Wu, J. Zhu, L. Zou, F. Xiao, Z. Su, C. Jiao, S. Pei, Z. Zhang, J. Qin, B. Xu, Y. Zhou, J. Xia and Z. Wang, *InfoMat*, 2024, **6**, e12553.
156 X. Fan, Z. Chen, D. Xu, L. Zou, F. Ouyang, S. Deng, X. Wang, J. Zhao and Y. Zhou, *Adv. Funct. Mater.*, 2024, **34**, 2404750.
157 M. Turunen, M. Brotons-Gisbert, Y. Dai, Y. Wang, E. Scerri, C. Bonato, K. D. Jöns, Z. Sun and B. D. Gerardot, *Nat. Rev. Phys.*, 2022, **4**, 219–236.
158 C. Palacios-Berraquero, D. M. Kara, A. R. P. Montblanch, M. Barbone, P. Latawiec, D. Yoon, A. K. Ott, M. Loncar, A. C. Ferrari and M. Atatüre, *Nat. Commun.*, 2017, **8**, 15093.
159 M. Koperski, K. Nogajewski, A. Arora, V. Cherkez, P. Mallet, J. Y. Veuillen, J. Marcus, P. Kossacki and M. Potemski, *Nat. Nanotechnol.*, 2015, **10**, 503–506.
160 S. Kumar, A. Kaczmarczyk and B. D. Gerardot, *Nano Lett.*, 2015, **15**, 7567–7573.
161 L. N. Tripathi, O. Iff, S. Betzold, Ł. Dusanowski, M. Emmerling, K. Moon, Y. J. Lee, S.-H. Kwon, S. Höfling and C. Schneider, *ACS Photonics*, 2018, **5**, 1919–1926.
162 M. Brooks and G. Burkard, *Phys. Rev. B*, 2018, **97**, 195454.
163 W. Zhao, Z. Ghorannevis, K. K. Amara, J. R. Pang, M. Toh, X. Zhang, C. Kloc, P. H. Tan and G. Eda, *Nanoscale*, 2013, **5**, 9677–9683.
164 Q. H. Wang, K. Kalantar-Zadeh, A. Kis, J. N. Coleman and M. S. Strano, *Nat. Nanotechnol.*, 2012, **7**, 699–712.
165 A. Srivastava, M. Sidler, A. V. Allain, D. S. Lembke, A. Kis and A. Imamoğlu, *Nat. Nanotechnol.*, 2015, **10**, 491–496.
166 T. T. Tran, K. Bray, M. J. Ford, M. Toth and I. Aharonovich, *Nat. Nanotechnol.*, 2016, **11**, 37–41.
167 J. A. Yang, R. K. A. Bennett, L. Hoang, Z. Zhang, K. J. Thompson, A. Michail, J. Parthenios, K. Papagelis, A. J. Mannix and E. Pop, *ACS Nano*, 2024, **18**, 18151–18159.
168 S. Chen, C. Wang, H. Cai, L. Ma, Y. Qu, Z. Liu, S. Wang, J. Zhan, Q. Tan, B. Sheng, X. Liu, X. Wang, X. Zhang, J. Xu, W. Gao and Q. Liu, *Matter*, 2024, **7**, 1106–1116.
169 Y.-M. He, G. Clark, J. R. Schaibley, Y. He, M.-C. Chen, Y.-J. Wei, X. Ding, Q. Zhang, W. Yao, X. Xu, C.-Y. Lu and J.-W. Pan, *Nat. Nanotechnol.*, 2015, **10**, 497–502.
170 T. Cai, J.-H. Kim, Z. Yang, S. Dutta, S. Aghaeimeibodi and E. Waks, *ACS Photonics*, 2018, **5**, 3466–3471.
171 W. Ming, B. Huang, S. Zheng, Y. Bai, J. Wang, J. Wang and J. Li, *Sci. Adv.*, 2022, **8**, eabq1232.
172 Y. Liu, A. N. Morozovska, A. Ghosh, K. P. Kelley, E. A. Eliseev, J. Yao, Y. Liu and S. Kalinin, *ACS Nano*, 2023, **17**, 22004–22014.
173 X. Jiang, X. Wang, X. Wang, X. Zhang, R. Niu, J. Deng, S. Xu, Y. Lun, Y. Liu, T. Xia, J. Lu and J. Hong, *Nat. Commun.*, 2022, **13**, 574.
174 M. Han, C. Wang, K. Niu, Q. Yang, C. Wang, X. Zhang, J. Dai, Y. Wang, X. Ma, J. Wang, L. Kang, W. Ji and J. Lin, *Nat. Commun.*, 2022, **13**, 5903.
175 C. Chen, H. Liu, Q. Lai, X. Mao, J. Fu, Z. Fu and H. Zeng, *Nano Lett.*, 2022, **22**, 3275–3282.
176 A. Weston, E. G. Castanon, V. Enaldiev, F. Ferreira, S. Bhattacharjee, S. Xu, H. Corte-León, Z. Wu, N. Clark, A. Summerfield, T. Hashimoto, Y. Gao, W. Wang, M. Hamer, H. Read, L. Fumagalli, A. V. Kretinin, S. J. Haigh, O. Kazakova, A. K. Geim, V. I. Fal'ko and R. Gorbachev, *Nat. Nanotechnol.*, 2022, **17**, 390–395.
177 Y. Zhou, D. Wu, Y. Zhu, Y. Cho, Q. He, X. Yang, K. Herrera, Z. Chu, Y. Han, M. C. Downer, H. Peng and K. Lai, *Nano Lett.*, 2017, **17**, 5508–5513.
178 Q. Liu, W. Wang, H. Sinhmar, I. Griniasty, J. Z. Kim, J. T. Pelster, P. Chaudhari, M. F. Reynolds, M. C. Cao, D. A. Muller, A. B. Apsel, N. L. Abbott, H. Kress-Gazit, P. L. McEuen and I. Cohen, *Nat. Mater.*, 2025, **24**, 109–115.
179 A. Branny, S. Kumar, R. Proux and B. D. Gerardot, *Nat. Commun.*, 2017, **8**, 15053.